Gaseous Mixtures/Detection Media Studies for the NEXT Experiment: A Contribution

Alexandre Nuno de Carvalho Amaral Garcia

Universidade de Coimbra
Faculdade de Ciência e Tecnologia
Departamento de Física

September 2012

Supervisor: Filomena Pinto dos Santos

Dissertation presented to the Faculdade de Ciências e Tecnologia part of the Universidade de Coimbra for a Master of Science Degree in Physics Engineering

To my family

Acknowledgments

I want to thank to Professor Filomena Pinto dos Santos, my supervisor that guided me during all my thesis, supporting me at all times and opening new doors for me. I would also like to thank to Pedro Neves for teaching how to work in the lab and for assisting me every time I needed. I am also thankful to Alexandre Trindade, who made my work possible, helping me in many situations. Also to Professor Carlos Alberto Nabais Conde that, with all his knowledge and experience, could find the motivation to spend time in the laboratory to help me. A special thank you to Professor Francisco Fraga, that guided me in solving some persistent problems in the electronics. To Augusto Cordeiro that took several evenings to come to the workshop and finish my work. I would also like to thank to everyone in LIP and workshops. To Alberto Blanco and Americo Pereira: they both made a good part of my experimental work possible. I would like to thank everyone in the NEXT collaboration in Valencia for giving me the chance of perform part of my work at IFIC. A special thank to Juan-José Gomez Cadenas for giving me the opportunity of going to IFIC, to Jose Díaz for welcoming me and to Nadia Yahlali for guiding me during my staying and for helping me with everything I needed. I would like to mention to my closest friends in Valencia that made me feel at home (despite the language!)

Thank you to GIAN staff for providing some necessary tools without which this work would have been very difficult.

I acknowledge a grant from Fundação para a Ciência e Tecnologia's program COMPETE through project "High Pressure Xenon doped mixtures for the NEXT collaboration" PTDC/ FIS112272/2009.

To my long-time friends, that kept trying to throw me off the rails in a daily basis. Thank you for keep reminding me what not to do!

I would also like to thank to Professor Filomena for all the personal advices, patience and for opening me the doors to the world of experimental Physics. Without her help, I would not be able to accomplish this thesis. I would like to thank to Filipa for the support she has given me and all the patience, especially during my stay in Valencia and in the last few weeks. Last, but not least, I would like to thank to all my family. My parents Isabel e José Alberto for all the efforts made providing me all I could ask for and more. To my grandparents António e Rosa that have always been there for me. To my brother and sister who have always been part of my life independently of the distance "separating" us. To my uncle António for small and big helps and care he has been providing me.

To the memory of my grandmother Etelvina.

Contents

Abstract

The purpose of this Master thesis is to contribute to the NEXT experiment (Neutrino Experiment with a Xenon Time Projection Chamber) by studying xenon based gaseous mixture properties. The work developed to study gaseous mixtures properties was based on three experimental setups: Ion Drift Chamber (IDC), Gas Proportional Scintillation Counter (GPSC) and Proportional Counter (PC).

With the IDC, measurements of Ne and N_2 ion mobilities in their parent gases were performed and the mobility of xenon ion in the Xe-N_2 mixture was also measured. These measurements were performed at low pressures (4 to 16 Torr) and reduced electric fields between 6 and 35 Td. For the Xe-N_2 mixture, the amount of dopant (N_2) ranged from 0 to 10%. The results attained for Ne and N_2 were in good agreement with other authors results. It could be concluded that adding nitrogen to xenon increases the xenon ion mobility. The results show that adding 10% of N_2 increases xenon ion mobilities by almost 6%.

The part of the work developed with the GPSC was the optimization of the first NEXT prototype - NEXT-0. The task proposed was to optimize the setup to overcome its major limitation: not being able to operate at high electric fields. Although not fully accomplished, the limitation was minimized, thus allowing for normal operation up to at least 1.5 bar. Another limitation that prevented normal operation was caused by non-desired radiation being detected, impairing the detection of the radioactive source. This limitation was fully overcome. Furthermore, data was acquired and it was possible to observe that pressure interferes with the resolution behaviour of the detector. The drift and electroluminescence fields applied are also correlated with the detector's resolution behaviour. In this way, the results obtained seem to show that more pressure improves resolution and that also diminishes the electroluminescence field requirements (it does not need to be as intense).

In the last part of the experimental work, a cylindrical proportional counter was projected, assembled and tested, and is working simultaneously and in parallel with a GPSC, in a specially designed Ultra-High-Vacuum system. Although the GPSC is not fully working yet, preliminary data has already been successfully obtained with the PC.

Chapter 1

Introduction

The purpose of this Master thesis is the study of gaseous mixtures based in xenon for radiation detection, as a contribution to the NEXT (Neutrino Experiment with a Xenon Time Projection Chamber). During the work developed in this thesis, different studies were performed using different experimental apparatus. For that reason, this work is divided in chapters according to the experimental apparatus used.

Chapter 2 refers to the work developed with an Ion Drift Chamber (IDC). This already existing experimental setup, allows to measure ions mobilities. Making use of the capabilities of the chamber, studies for different pure gases and gas mixtures at different pressures and under variable electric fields were made.

The following chapter (NEXT-0) refers to the work performed with the first prototype of NEXT. NEXT-0 is a Gas Proportional Scintillation Counter (GPSC) and the focus of this part of the work was on having the system working for future studies.

The last experimental apparatus used, was a Cylindrical Proportional Counter (CPC). This chamber was projected and built to study recombination effects of xenon mixtures at pressures above the atmospheric pressure. To perform these studies, the system was projected to have the CPC working simultaneously and in parallel with a GPSC.

Due to the relevance of NEXT experiment to this work, it will be included in this introduction a section that will put in evidence the objectives and the problems still existing in the referred experiment. Additionally, at the beginning of each chapter, it is mentioned how each study is related to NEXT.

1.1 NEXT Experiment

The NEXT project is an experiment that proposes to use a Time Projection Chamber (TPC) to detect the neutrinoless double beta decay. This TPC will be located at the Canfranc Underground Laboratory in Spain [1]. It has been predicted that two types of double beta decay ($\beta\beta$) may occur: the regular decay (with two neutrinos emission $2\nu\beta\beta$) and the neutrinoless emission $0\nu\beta\beta$. To seek $0\nu\beta\beta$ in NEXT, a 100kg of ^{136}Xe enriched gaseous xenon will be used.

The actual mass of xenon may be more than 100kg, in order to increase the probability of detecting the desired decay.

A major part of this experiment is related to the neutrino's nature, which is one of the still unsolved problems in Physics. There is experimental evidence that neutrino oscillates, which implies that it is a massive particle [2]. As in the *Standard Model* it was introduced as a massless particle, it may be required to extend the model to accommodate it. Despite the experimental evidence that neutrino oscillates, its mass is still unknown and only an upper limit of about 280 meV has been estimated by different experiments and cosmological considerations [3]. The $0\nu\beta\beta$ decay detection is one of the experimental methods that might reveal the neutrino's nature and give values for its mass. Detecting this decay, implies that neutrinos are Majorana particles, *i.e.*, they are their own anti-particles. Furthermore, $0\nu\beta\beta$ confirmation would be an attractive explanation for the tinny mass of neutrinos and could help finding out why matter prevails over anti-matter, proving that total lepton number is not a conserved quantity in nature [4, 5].

Double beta decay is a rare decay that can only be observed if the corresponding simple beta decay (only one beta particle emitted) is energetically forbidden. Hence, only few isotopes of few elements meet this condition. The regular double beta decay ($2\nu\beta\beta$) occurs as a common two step beta decay but simultaneously. It produces an electron pair spectrum, as the one in Figure 1.1 [2].

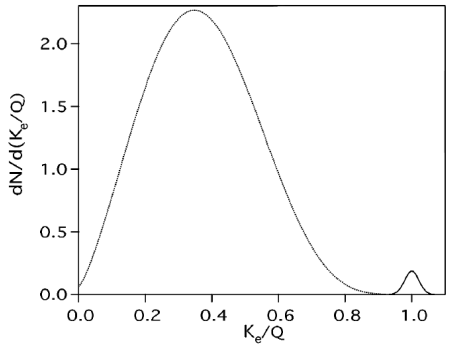

Figure 1.1
Double beta decay spectrum
The large peak is the $2\nu\beta\beta$ process and the small peak the $0\nu\beta\beta$ process (taken from [6])

If the massive neutrinos are Majorana particles the $0\nu\beta\beta$ can occur and the corresponding energy spectrum would be one peak at the value $Q_{\beta\beta}$ (2458keV) [4, 5]. $Q_{\beta\beta}$ is the energy difference between parent-daughter nuclei [7]. In Figure 1.1 the two double beta decay are depicted: the big peak is the one with two neutrinos and the small one the neutrinoless. Thus, it is of paramount importance to be able to resolve these two peaks in order to detect the double beta decay without emission of neutrinos. Additionally, this experiment, or any other that aims to detect the double beta decay, must be sensitive to lifetimes longer than 10^{25} years - consistent with effective Majorana neutrino masses smaller than 100 meV [5].

As mentioned before, NEXT is an experiment based on xenon. This gas is going to be used simultaneously as detection medium and as radioactive and there are many reasons for this option. First, the neutrinoless double beta decay can theoretically occur in xenon. Also, the ^{136}Xe is the only noble gas isotope that can decay in double beta and has a natural abundance rather high (8.86%). Furthermore, it is a noble gas that provides excellent intrinsic energy resolution as detection medium. Adding to these advantages, this gas has a relatively cheap and simple enrichment technique. Moreover, xenon has no other long-lived radioactive isotopes that could become a background and ^{136}Xe has a rather high $Q_{\beta\beta}$. This is an advantage when comparing to isotopes with lower values of $Q_{\beta\beta}$, since radioactive backgrounds are lower at this energy region. The value of the $Q_{\beta\beta}$ is important for choosing an isotope not only for that reason, but also because the decay rate is proportional to $(Q_{\beta\beta})^5$. As ^{134}Xe has a lower $Q_{\beta\beta}$ value, it is less attractive for this experiment. Another relevant reason for choosing xenon, is that neutrinoless double beta decay events leave a ionization track in this gas. This is a topological signature of this decay, very useful to perform background rejection [5].

Current Neutrinoless Double Beta Decay Search

The NEXT experiment is not the only experiment looking for the neutrinoless decay. A few other experiments are also running, using different techniques and different elements/isotopes such as ^{130}Te,$^{76}\,Ge$,$^{150}\,Nd$,$^{82}\,Se$. Besides NEXT, experiments like CUORE, KamLand-Zen and EXO seem capable of exploring the *Effective Majorana Mass*, $m_{\beta\beta}$, of the electron neutrino in regions around 100meV [8]. Other experiments such as GERDA, SNO+ or SuperNEMO are searching for the same decay type, but they don't seem capable of reaching these $m_{\beta\beta}$ regions.

Upon the capability of scaling the technologies to large masses, all of the mentioned experiments might be able to explore the 100meV scale. NEXT, CUORE, KamLAND-Zen and EXO are already capable of exploring this energy scale and, if also scalable, they may be able to explore regions below the 50 meV $m_{\beta\beta}$ [8].

1.1.1 NEXT $0\nu\beta\beta$ Detection

The detection of the neutrinoless double beta decay in NEXT will be made by means of a time projection chamber. This chamber is basically a more complex and larger version of a Gas Proportional Scintillation counter that has an energy plane and a tracking plane (Figure 1.2).

The neutrinoless decay can be represented by:

$$ {}^{A}_{Z}X \rightarrow {}^{A}_{Z+2}\,Y + 2e^{-} \tag{1.1} $$

The two electrons emitted by the neutrinoless decay, interact with the high-pressure xenon transfering their energy to the medium by means of excitations and ionizations. The excitations produce scintillation light (Primary Scintillation) peaked at $\sim$ 175nm, which will be detected. The ionization effect produces electrons. As a weak electric field is applied, the electrons

drift along it until they reach a region where a stronger electric field is applied - the electroluminescence region. Once in that region they produce electroluminescence light (secondary scintillation). This light, emitted isotropically, will be detected in both planes. The PMTs in the energy plane use this light to measure the energy of the initial interacting particles and the Silicon Photomultipliers (SiPMs) in the tracking plane will reconstruct the path of the initial electrons. The figure below illustrates the process described before:

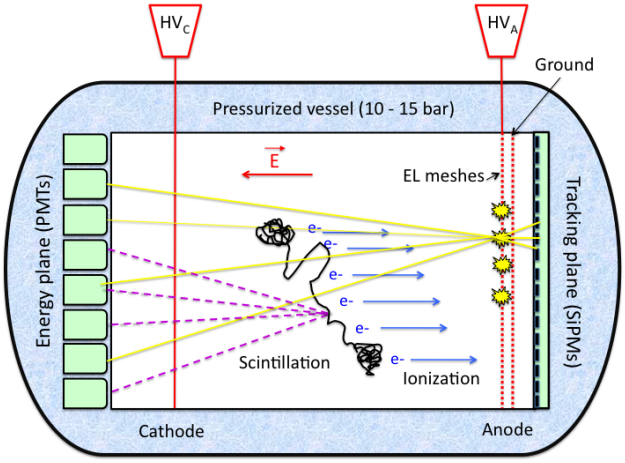

Figure 1.2
NEXT TPC scheme (taken from[5])
Energy plane depicted on the left and the Tracking plane on the right; HV grids (Cathode and Anode) and the Ground are also illustrated

In this chamber, the primary scintillation light is used as a trigger for setting the start-of-event, which allows to determine the coordinate "z" of the particle along the drift region. The combination of both planes and respective roles, provide excellent energy resolution as well as topological information, which allows efficient background rejection [5].

1.1.2 Unavoidable Detection Requirements

Neutrino-less double beta decay experiments aim at measuring the $0\nu\beta\beta$ peak at the end point of the $\beta\beta$ energy spectrum. For that reason, an optimal energy resolution must be attained, with the detection medium and the technique playing a crucial role. The xenon gas was choosen as a detection medium in NEXT because of its several advantages. However, the possibility of adding dopants to it is being studied, because dopants such as CH_4, CF_4 and TMEA may be a valuable help in increasing both energy and tracking resolution.

NEXT experiment aims at measuring the energy with a resolution of at least 1% FWHM at $Q_{\beta\beta}$. NEXT-DEMO used the 662 keV photoelectric peak for ^{137}Cs to measure the energy resolution, which was found to be close to 1% FWHM [5]. This resolution if extrapolating for $Q_{\beta\beta}$, assuming $1/\sqrt{(E)}$, gives an energy resolution of $\sim 0.5\%$ FWHM [5].

In order to detect the eventual $0\nu\beta\beta$ peak, is not enough to reach the mentioned energy resolution, as well as all background in the region $Q_{\beta\beta}$ must be avoided. That is the same as saying that all interactions with energies near $Q_{\beta\beta}$ value must be avoided and even the $2\nu\beta\beta$ spectrum can cause background in that energy region (although it has a long decay life-time of about 2.38×10^{21} years [9]).The most dangerous radioactive contaminants of the experiment are the isotopes ^{208}Tl and the ^{247}Bi with decays of 2614 and 2447 keV respectively. Some of other relevant background sources expected are [4]:

- Radioactive contamination from the detectors materials
- Radioactive contamination from the laboratory walls (environmental radioactive contamination)
- Radioactive contamination from the protections against radioactivity
- High energies photons due to interactions with muons
- Neutron activation

In order to perform background rejection, both tracking and energy plane are used. If the energy resolution is good enough, most of the spurious activity in the detector for the energy region of $Q_{\beta\beta}$ is rejected using the energy plane. As the neutrinoless double beta decay signal events have a unique topology and appear distributed uniformly in the active volume, almost all charged background entering the detector are going to be eliminated by the tracking plane.

However, the materials used in NEXT and the rocks where the laboratory stands also emit radiation. In order to shield the detector from that type of radiation, a Pb castle is going to be built. Additionally, it is important to perform a careful choice of materials and control the amount of each material used. The NEXT collaboration estimates that background rate to be $8 \times 10^{-4}\,\text{counts} \cdot \text{keV}^{-1} \cdot \text{kg}^{-1} \cdot \text{year}^{-1}$ [5].

For all that was mentioned, it is easy to understand that this experiment has many challenging goals. Some of them, such as the energy resolution goal, have already been accomplished. In an experiment as NEXT, every detail counts and the work developed in this Master thesis falls within the NEXT scope, as it may provide optimization in the experiment.

1.2 Relevant Physics Concepts

1.2.1 Scintillation Light

Upon electron excitation, xenon is known to emit electroluminescence (EL). In a detector based on EL production it is relevant to distinguish between *Primary Scintillation* and *Secondary Scintillation* light.

Primary Scintillation & Secondary Scintillation

There are differences between primary scintillation and secondary scintillation light, although the light emitted has the same characteristics, as the phenomena involved are the same.

When an incident particle interacts with neutral Xe atoms it may undergo one of three processes: elastic, ionization or excitation collisions. The three will occur according to the probabilities at the relevant energy. If excitation occurs at any pressure above few hundred Torr, it is likely to happen a three-body collision by means of which an excited Xe molecule (excimer) will be produced. This molecule, when vibrationally relaxed, returns to the ground state emitting a photon of a certain characteristic wavelength (∼175 nm). This is a naturally occurring process during the energy degradation of high energy electrons and is called Primary scintillation. However, this process may be enhanced upon applying the conditions that favour its occurrence.

In the sequence of a photon absorption event in the medium (Xe), an electron cloud is produced. The ensemble of electrons will be losing their energy upon colliding with media atoms. If properly guided by means of a low electric field, the electrons can be driven into a region where settings favour electroluminescence production. Thus the only difference between primary and secondary scintillation are the conditions surrounding its production: if it comes from a spontaneous electron atom collision then it is primary scintillation; if, on the other hand, the events are induced by a suitably chosen electric field then the scintillation is said to be secondary.

For pressures above few hundred Torr, the processes taking place after the xenon atom has been excited are the following [10]:

$$\begin{aligned} Xe^* + 2Xe &\rightarrow Xe_2^{**} + Xe \\ Xe_2^{**} + Xe &\rightarrow Xe_2^{*} + Xe \\ Xe_2^{*} &\rightarrow Xe + Xe + h\nu \end{aligned} \tag{1.2}$$

where Xe^* is an excited Xe atom, Xe_2^{**} an excimer in a non-relaxed vibrational state and Xe_2^* an excimer in the lowest excited state. $h\nu$ is the photon emitted by the de-excitation of the excimer.

In the case of NEXT it is important to be able to distinguish between primary and secondary scintillation light, since they will have different roles within the experiment.

1.2.2 ω-value & Fano factor

The $\omega -$ value is the mean energy required to form an electron-ion pair in a certain medium. ω depends on the medium and the energy of the incident particle [11]. At low energies (electron energy below 50 keV) this value increases as the incident particle energy decreases. At high energies it reaches a constant value. ω is defined as:

$$\omega = \frac{E_{ir}}{\overline{n}} \tag{1.3}$$

where E_{ir} is the energy of the incident radiation and $\overline{n}$ is the mean number of primary electrons produced by an ionizing radiation when absorbed in the gas [12, 13].

The *Fano* factor (F) is an empirical factor. This factor accounts for the fact that the number of electron-ion pairs produced by an incident particle in a medium deviates from pure Poisson statistics. This deviation is due to correlation factors in the electron production mechanism [14]. For each gas and energy of interacting particle, F states how much smaller the variance is than the predicted Poisson variance [15]:

$$F = \frac{\text{observed variance in } \overline{n}}{\text{Poisson predicted variance}} \tag{1.4}$$

As it can be seen by looking to the above equation, F has a value between 0 and 1.

Energy Resolution Limits

One of the most relevant characteristics of radiation detectors is the energy resolution. Energy resolution translates the minimum difference in energy of two different events so that a given detector can distinguish and detect them as separate peaks.

In a radiation detector, one of the parameters that affects the energy resolution is directly related to the statistical fluctuations in the number of electrons produced by the incident radiation. This is why Fano factor and ω-value limit the intrinsic energy resolution of any type of radiation detector based on ionization.

As the variance of $\overline{n}$ is given by:

$$\sigma_n^2 = F \cdot \overline{n} \tag{1.5}$$

and the intrinsic energy resolution, R, is given by :

$$R \cong 2.355 \times \frac{\sigma_n}{\overline{n}}$$

it is possible to establish the intrinsic energy resolution due to the parameters ω and F for x-rays of energy E_{ir} [12]:

$$R \cong 2.355 \times \sqrt{\frac{F\omega}{E_{ir}}} \tag{1.6}$$

Both F and ω have a major role in limiting the energy resolution in any detector that uses gas as detection medium, and, although these are not the only relevant factors, they establish a lower limit on the final energy resolution attainable.

Chapter 2

Ion Drift Chamber

This chapter presents the work performed with an Ion Drift Chamber (IDC). This experimental apparatus was already developed [16] and it allows to measure the mobility of ions in a gaseous atmosphere. In this work we perform measurements with different gases and gas mixtures. Drift velocities of ions were measured for different values of E/N and at different pressures – lower than atmospheric pressure.

This study can be useful for the neutrinoless double beta decay search, since if a suitable mixture is found it reduces the xenon diffusion and it may provide means to detect the Barium daughter nucleus. The Barium daughter nucleus is a product of the $^{136}Xe\,\beta\beta$ decay and it can be used to perform *Barium tagging* [17], which would allow to eliminate all background but the intrinsic $2\nu\beta\beta$ [4]. For that reason, the purpose of this research is to provide a better understanding of the effect of dopants in the mobility of xenon ions.

2.1 Introduction

The measurement of ions' properties is relevant in many applications. With the emergence of the Ion Mobility Spectrometry (IMS) method, that allows the detection of molecules based on the mobility of ions in a certain carrier gas, developments were made within military scope such as detection of explosives, drugs and pollutant [18]. The technology allows for small, portable and robust IMS equipment that can be used in many fields. One of the most popular uses is analysers that exist in airports all-around the world for detection of explosive traces inside the passengers' luggage.

In our case, the interest of measuring ions' drift velocity rose from the need to study the electrical signal produced in gaseous radiation detectors. As ions drift away from the anode, and while they are not collected in the cathode, they induce a signal at the anode much slower than the one produced by the electrons (collected at the anode). Therefore, in order to fully understand this electronic signal, one needs to study various properties related with the transport of the ions in the gases used in gaseous radiation detectors. The ions drift velocity study with this ion drift chamber was already made for Ar, Kr, Xe [16, 19], and admixture P-10

$(90Ar - 10CH_4)$ [20].

When a group of ions moves within a weakly ionized gas under the effect of a uniform electric field, the ions collide with neutral gas atoms losing energy at each collision and gaining/losing energy from the field. When the average collisional energy loss equals the average energy gained from the electric field, the equilibrium condition has been attained. In this case we can define drift velocity as being the average velocity of the group of ions:

$$v_d = KE \tag{2.1}$$

where K is the ions' mobility and E the intensity of the drift electric field. It is common to use the concept of reduced mobility K_0 that facilitates the comparison of results between authors, that often perform experiments in different conditions of pressure and for different electric fields. The relationship between K and K_0 is given by:

$$K_0 = KN/N_0 \tag{2.2}$$

where N is the gas number density and N_0 is the Loschmidt's number ($\mathrm{N_0} = 2.6868 \times 10^{25}\ \mathrm{m^{-3}}$); mobility measurements are commonly shown as a function of the reduced electric field E/N in units of Townsend ($1\mathrm{Td} = 10^{-21}\ \mathrm{Vm^{-2}}$).

2.1.1 Langevin Limit

According to the Langevin's theory, when an ion moves in a gaseous medium composed of neutral atmos/molecules, a limiting value for ion mobility is reached when the repulsion cross section for the interaction between the ion and the neutral becomes negligible when compared to the polarization effect. In many situations the Langevin limit has proved to describe correctly the mobility of ions in the low-field region. For that reason, authors that measure ion mobilities, not seldom choose to calculate by extrapolation the limiting value of the reduced mobility of the ion when $E/N \to 0$. They then compare the value Langevin's limit value to the value obtained by experimental measurements to evaluate the accuracy of the experimental method. In our work, we have also calculated this value in order to compare it to our experimental results. Using this extrapolation we can find the reduced mobility of an ion when $E/N \to 0$ simply:

$$K_0 = \frac{13.88}{\sqrt{\alpha\mu}} \tag{2.3}$$

where α is the neutral polarizability in $\mathrm{\AA}^3$ and μ is the ion-neutral reduced mass in a.m.u. [21].

The principle of measuring the ions' drift velocity with this technique is based on a simple concept: the average velocity of a group of ions that moves in a gaseous medium under the influence of a uniform electric field, is determined by measuring the time that they take to travel a known distance. Some difficulties may arise when there are different ion types (including impurities) simultaneously present in the experimental set up.

Measuring the ion's drift velocity is based on a simple concept. We can obtain that information measuring the average time that ions take to drift across a given distance within a gas. However, difficulties may arise when different types of ions (impurities included) are present at the same time within the experimental set up. For a better understanding of the work developed in this chapter, some notions are going to be presented.

2.1.2 Blanc's Law

Blanc's Law is a relation for binary gas mixtures. This law gives the reduced mobility of a certain ion in a gas mixture, based on the reduced mobility of that ion in each of the pure gases. This law is a result of a research done by A. Blanc in 1908, studying binary mixtures such as H_2 and CO_2 [22]. In that research it was found that:

$$\frac{1}{K_0} = \frac{f_1}{K_{01}} + \frac{f_2}{K_{02}} \tag{2.4}$$

where K_0 is the mobility of the ion in a mixture, K_{01} and K_{02} the reduced mobility that same ion in the "pure gases" #1 and #2 respectively, *i.e.*, the ion reduced mobility that is expected to be observed in an 100% atmosphere of each gas present in the mixture; f_1 and f_2 are the fraction of each gas in the mixture.

2.2 Experimental Setup

The experimental set up used consists of a stainless still vessel, a Gas Electron Multiplier (GEM), covered with a 250nm thick CsI film, an UV flash lamp and a double grid (G_1 and G_2). In the figure below we can see a schematic representation of the physical processes involved in this set up:

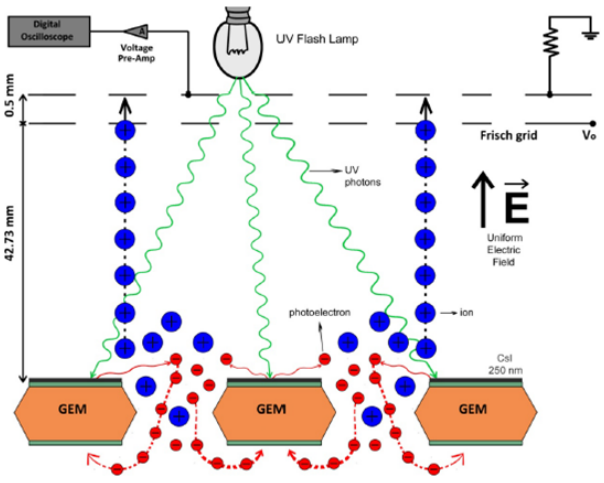

Figure 2.1

Schematic representation of the physical processes that lead to the production and detection of ions [23]

Photons from the pulsed UV flash lamp which hit the CsI layer cause the release of photoelectrons from the CsI photocathode. When proper high-voltage (HV) is applied between the GEM's two surfaces a strong electric field is produced inside the holes of this structure. The photoelectrons produced in the GEM's top surface, experience an intense electric field that points from the top surface to the bottom surface of the GEM, which forces the electrons to enter the GEM's holes. After entering these holes, if they get enough energy they ionize the surrounding gas atoms. As we can control the voltage across the GEM in practice we are controlling if the electrons will or will not get enough energy to ionize the gas atoms. While the electrons produced are later collected in the GEM's bottom electrode, the cations drift in the opposite direction and some of them will enter the drift region, towards the double grid where they are collected.

The G_2 grid works as a Frisch's grid, preventing the ions to induce signal in the grid G_1 while they move in the drift region, so that they will only induce signal in G_1 after they cross G_2. A schematic view of the vessel can be observed in figure 2.2:

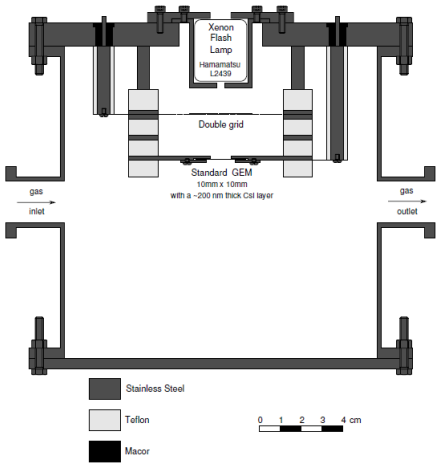

Figure 2.2

Schematic view of the Ion Drift Chamber used (taken from [18])

The vessel consists of two flanges compressed against a stainless steel cylindrical body with a 150 mm diameter, with Viton O-rings sealing it. The MACOR pieces are used to insulate the feedthroughs, one for signal collection and the other for the voltage biasing. In the figure, only two of those feedthroughs are depicted.

When measurements are going to be performed, the vessel is vacuum pumped until the pressure reaches a magnitude of $10^{-6} - 10^{-7}$ Torr, using a turbo-molecular pump (Edwards EXPT pumping station connected to an Edwards 1575 Pressure Display). Then it is filled up with ultra-pure gases (purity $\geq$ 99.9999 %). The gas pressure is controlled by an Edwards Barocel 600AB Trans (up to 100 mBar). The distance between the double grid and the GEM, the drift distance, is set to 42.37 ± 0.2 mm. It was set using Teflon spacers. Two 2 mm thick field rings were implemented between the double grid and the GEM in order to ensure the

uniformity of the electric field in the drift region.

The GEM electrodes and the field ring were connected to a high voltage power supply, CAEN-2 model N471. The double grid consists of two meshes within a short distance of each other, G_1 and G_2, and they are separated by a MACOR piece with 0.5 ± 0.1 mm thickness. The G_2 grid was connected to a precision dc power supply (Thandar TS2022S 30V). The lamp is a Hamamatsu Xenon UV flash lamp, model L2439, and it was used at 10Hz, with pulse duration shorter than 500ns. The electric pulse induced in G_1 feeds a custom-made pre-amp and is then recorded in the oscilloscope (Tektronik TDS 1012) that allows the continuous calculation of the average of up to 128 pulses. That data is processed afterwards in a PC.

In this technique, in opposition to the majority of the ion mobility techniques, no radioactive sources are used as ion sources. The ion source is the GEM working together with the UV flash lamp, in such a way that the ions are produced at the GEM in the avalanche region (GEM holes). This region is a really thin region (typically 60 µm thickness, 70 µm diameter holes and a pitch of 140 µm) when compared with the drift distance, thus the ions' initial position is known with great accuracy.

2.2.1 Limiting Electrons Energy

One feature that this experimental apparatus has that is relevant to mention, is that we can control the energy acquired by the photoelectrons inside the GEM holes. In other words, we know the maximum energy that the electrons produced in the photocathode can gain, thus we know if the photoelectrons are able to ionize the surrounding atoms or not. What happens inside this experimental system is that for a $V_{GEM} = x$V the maximum energy that can be gained by the photoelectrons will be x eV.

2.2.2 System Operation

When I started working with this experimental set-up, the system was already in use. For that reason I have experimented an adaptation period before I fully understood the system and was able to try to improve what was being done. The first study that I have performed with this experimental set-up was the measurement of Ne ions drift velocities. But before reaching a final value for the Ne drift velocity, I have performed some other measurements to understand how the system worked.

The procedure to perform measurements is simple. We have a dual-stage high-purity gas regulator that allows filling the vessel with the desired gas. In this experimental apparatus, when working with mixtures, the filling up must be done with one type of gas at each time. It is not possible to adjust the ratio of each gas after the filling is completed. That means that after the second gas is allowed in it is not possible to re-introduce more gas from the first type without compromising the mixture true ratio.

After having the desired gas inside the chamber, the measurement should be done quickly, since after typically 3 minutes, and depending on the gas used, the signal starts to deteriorate.

The oscilloscope needs just a few seconds to perform a 128 signals average and to save the file. This means that is possible to perform more than one measurement for each gas filling under the mentioned 3 minutes. To perform more measurements the system must be evacuated and the process re-done.

Another variable that is important to keep monitored is the temperature. It was possible to observe that for the same conditions, varying the temperature changes the ions mobilities. Briefly, from 18 °C to just under 25 °C it does not seem to be any change in ions mobilities, besides the expected statistical deviation. However, for temperatures over 25 °C the ions mobilities would vary in a random way.

The suspicions are that these variations are due to outgassing. We already knew that to have the system in proper conditions to measure ions mobilities, we should perform 7/8 filling ups followed by evacuations, independently from the vacuum reached. Only after that procedure, reproducible results were attained. What we could see during these filling ups, was that in the first couple of measurements we would have a large peak that after the 3^{rd} or 4^{th} measurement would become two peaks of the same size, and one of them would decrease, filling after filling, until we reached a state from which we could no longer improve the relation between the two peaks. The typical result is a main peak and a small lump on the side. In nitrogen this effect was more evident. Furthermore, if we work more days in a row with the same gas, we need fewer fillings to reach the same point. When we had the system not being used for one week, in the first two days instead of the usual 7/8 fillings we would need 10 or even 12 fillings.

Among the three gases used (Ne, N_2 and Xe) it was possible to observe that xenon deterioration was much slower than for other gases. A possible explanation is that N_2 and Ne molecules/ions would attach to impurities present in the detector while xenon, a bigger inert gas, would not.

Also working with the Xe-N_2 mixture it was possible to understand that the Xe had cleaning properties, *i.e.* , that after working with Xe, even when performing measurements with nitrogen, the system would be cleaner than when working only with nitrogen. That was visible because from one day to the other the number of fillings needed would not be as high as when working only with nitrogen, possibly due to adsorption in the detector's walls.

2.3 Results & Discussion

In this section it will be presented and discussed the results obtained with this experimental system for two pure gases and one gas mixture: Ne, N_2 , and $Xe - N_2$ mixture.

2.3.1 Neon

We measured the reduced mobilities of the atomic, Ne^+, and dimer, Ne_2^+, ions in Ne, under different pressures and reduced electric fields, at 300 K [19]. Extrapolation to zero field yields values of 4.4 $cm^2V^{-1}s^{-1}$ for Ne^+ and 6.2 $cm^2V^{-1}s^{-1}$ for Ne_2^+. Ne^+ ions are converted to Ne_2^+

by a three-body reaction and this reaction rate constant was measured for reduced electric fields in the 8 to 12 Td range with an average value of $5.6 \pm 0.1 \times 10^{-32}\,\mathrm{cm}^6\mathrm{s}^{-1}$.

In the figure below we can see depicted a typical pulse:

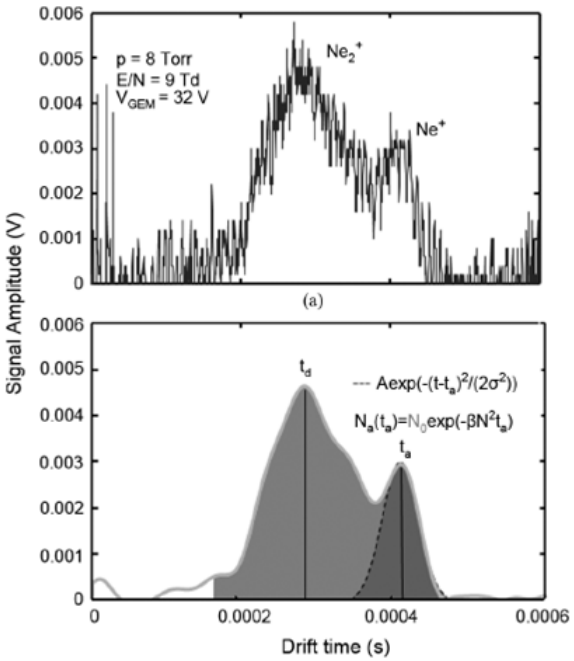

Figure 2.3

a) Average of 128 pulses for Ne, 8 Torr, 9 Td and V_{GEM}*=32V*

b) Signal a) after removing its high frequency noise. Total grey area is proportional to the total number of ions N_0*. The darker area is the Gaussian curve fitted to the atomic ion peak and is proportional to the number of atomic ions [19]*

The results obtained can be seen in the following figures:

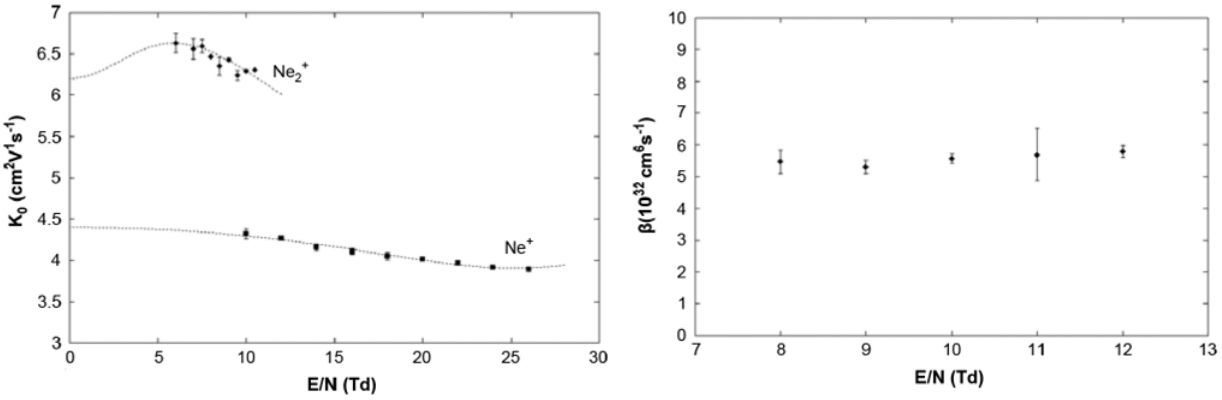

(a) **(b)**

Figure 2.4

a) Reduced mobilities of the atomic (Ne^+) and dimer (Ne_2^+) ion in Ne. Results for pressures between 4 and 10 Torr

b) Rate constant β for the $Ne^+ + 2Ne \rightarrow Ne_2^+ + Ne$ reaction. Measurements between 6 and 9 Torr [19]

In the figures 2.4a and 2.4b above and in tables 2.1a and 2.1b presented below, it is possible to see the reduced mobility of both neon ions and the rate of reaction of the conversion of Ne^+ ions into Ne_2^+ ions:

Table 2.1

a) Reduced mobilities for Ne^+ and Ne_2^+ ions in Ne at 300K

b) Reaction Rate of $Ne^+ + 2Ne \rightarrow Ne_2^+ + Ne$ at 300K

E/N (Td)	K_0 (cm^{2}V^{-1}s^{-1})	
	Ne_2^+	Ne^+
6	6.63±0.12	---
7	6.56±0.12	---
7.5	6.59±0.08	---
8	6.47	---
8.5	6.35±0.11	---
9	6.43±0.02	---
9.5	6.24±0.06	---
10	6.30±0.02	4.32±0.06
10.5	6.31	---
12	---	4.26±0.01
14	---	4.15±0.04
16	---	4.11±0.04
18	---	4.05±0.05
20	---	4.01
22	---	3.97±0.02
24	---	3.91
26	---	3.89

(a)

E/N (Td)	β (×10^{-32} cm^{6}s^{-1})
8	5.5 ± 0.4
9	5.3 ± 0.2
10	5.6 ± 0.2
11	5.7 ± 0.8
12	5.8 ± 0.2

(b)

Ions Mobility

As mentioned before, the mobility of two ions were measured. In figure 2.3 the top part is the signal from the oscilloscope. As can be seen, the signal has two peaks. In the same figure,

in the bottom part the high frequency noise was removed. Additionally the atomic ion peak was fitted to a Gaussian function that is represented by the dashed line. The centroid of the fit represents the average drift time of the Ne^+ ions.

Depending on the experimental conditions, there will be one ion species dominating the other. The atomic ion is dominant at lower pressures and higher reduced electric fields and, in contrast, the dimer ion is dominant at higher pressures and lower electric fields. For that reason the measurements to obtain the mobility of the dimer ion were performed at pressures of 7.5 to 10 Torr and reduced electric fields of 6 to 10.5 Td, while the atomic ion's measurements were performed with pressures starting at 4 Torr and reduced electric fields starting at 10 Td.

In figure 2.3 the Ne_2^+ ion corresponds to the t_d (dimer) peak and the Ne^+ ion corresponds to the t_a (atomic) peak. These peaks maxima allow the calculation of the average velocity of the ions reaching the collecting grid.

To obtain our experimental results we did not considered pressures below 4 Torr. For this range of pressures the mobility measurements begin to deviate from what one would expect. Having noticed that deviation and considering the drift distance and the E/N values we work with, we believe that a steady-state could not be attained due to an insufficient number of ion-neutral collisions. Additionally, it is possible to notice that no results are presented for E/N under 6 Td or over 26 Td. On the low end values of E/N (under 6 Td), the ions have a very long drift time, which increases the probability of colliding with impurity molecules. On the other end, high values of E/N, discharges occurrences make it impossible to perform measurements. For those reasons we restricted our work to the 6 to 26 Td.

Now, considering the equation 2.3 we can calculate the reduced mobility values of Ne^+ and Ne_2^+ and we obtain 6.9 and 6.0 $\mathrm{cm^2V^{-1}s^{-1}}$, respectively, since $\alpha = 0.394\,\mathrm{\AA}^3$ for Ne [24]. We used the same fitting functions as in Beaty and Patterson [25] in order to make the extrapolation of the mobilities of both ions when $E/N \to 0$. These authors discuss both functions taking into account that K_0 must be an even function of E/N and that K_0 goes as $E/N^{-1/2}$ for high E/N values [19]. Two functions were used, one for the atomic ions and another for the dimer ions [19]. For the Ne^+ we have that:

$$K_{0a} = \frac{a_0}{\left(1 + a_1(\frac{E}{N})^2 + a_2(\frac{E}{N})^4\right)^{\frac{-1}{8}}} \tag{2.5}$$

where $\mathrm{a_0 = 4.4\,cm^2V^{-1}s^{-1}}$, $a_1 = -0.00193\mathrm{Td}^{-2}$ and $a_2 = 1.51 \times 10^{-6}\mathrm{Td}^{-4}$.

For dimer ions:

$$K_{0d} = b_0 \left(\frac{1 + b_1(\frac{E}{N})^2}{1 + b_2(\frac{E}{N})^2 + b_3(\frac{E}{N})^4}\right)^{1/4} \tag{2.6}$$

where $b_0 = 6.2\,\mathrm{cm^2V^{-1}s^{-1}}$, $b_1 1 = 0.0355\ \mathrm{Td}^{-2}$, $b_2 = 0.0139\ \mathrm{Td}^{-2}$ and $b_3 = 0.00019\ \mathrm{Td}^{-4}$. In the Figure 2.4a it is possible to see these two functions represented by dashed lines.

Observing table 2.2 we can see that the results for the reduced mobility of the Ne^+ ion are in good agreement with other values on this table but not in agreement with the Lagevin's

limit. This can be explained by the non-validity of the Langevin formula when the ions are involved in reactions with the atoms of the gaseous medium. In this case, the atomic ions move along the drift region colliding with gas atoms which slows them down by a symmetric charge transfer process [19]:

$$Ne^+ + Ne \rightarrow Ne + Ne^+ \tag{2.7}$$

This reaction explains the reason why atomic ions are slower than the dimer ones, in spite of the size, and why the value predicted by the Langevin formula is not close to the one obtained experimentally. The probability that Ne^+ ions undergo symmetric charge transfer process with medium atoms is high, while for Ne_2^+ the probability of being involved in a similar interaction is rather low.

Reaction Rate Coefficients

We have measured the rate of reaction for pressures between 6 to 9 Torr and reduced electric fields ranging from 8 to 12 Td. As for reactions happening within the detection medium, as mentioned before, the atomic ions are converted to dimer ions. This happens by means of a three body reaction [19]

$$Ne^+ + 2Ne \rightarrow Ne_2^+ + Ne \tag{2.8}$$

Assuming that only Ne^+ ions are created in the GEM holes (*i.e.*, neglecting the production of Ne_2^+ ions by associative ionization), the number of atomic ions, N_a, varies with time according to:

$$\frac{dN_a}{dt} = -\beta N_a N^2 \tag{2.9}$$

In the above equation, β is the rate constant of the reaction 2.8, N the gas number density. Representing the total number of ions (Ne^+ and Ne_2^+) by N_0, then the number of atomic ions, N_a, at a given time t is given by:

$$N_a(t) = N_0 exp(-\beta N^2 t) \tag{2.10}$$

Based on this equation and on the data taken, we consider the total area, A_0, under the two peaks (grey area in figure 2.3), instead of considering the number of ions. This area is proportional to the total number of ions collected, N_0.

Thus, the number of atomic ions, N_a, at an instant t_a is proportional to the area bellow the Gaussian curve in the same figure. The area, A_a, is represented by the dark grey part and t_a is also the centroid of the Gaussian. Replacing the constants by the new proportional constants, in equation 2.10, we will have that:

$$A_a(t_a) = A_0 exp(-\beta N^2 t_a) \tag{2.11}$$

and we can get the reaction rate coefficient values, β:

$$\beta = -ln\frac{\left(\frac{A_a(t_a)}{A_0}\right)}{(N^2 t_a)} \tag{2.12}$$

In table 2.1b and figure 2.4b we present the values obtained and we can see that they do not depend on *E/N*. In table 2.2 we compare our results with results from other authors; we can conclude that the agreement is quite satisfactory.

Table 2.2

Zero field mobilities and reaction rates for conversion of Ne^+ ions into Ne_2^+ ions in Ne

Reference	**K_0 ($cm^2\ V^{-1}\ s^{-1}$)**		β	**T (K)**
	Ne^+	**Ne_2^+**		
Hornbeck [26]	4.4	5.85	—	300
M.A. Biondi [27]	4.0	6.5	—	300
L.M. Chanin [28]	4.2	6.5	—	300
M.J. Mulcahy [29]	3.9	7.5	—	300
H.J. Oskam [30]	4.1	6.5	—	300
E.C. Beaty [31]	4.0	—	5.8 ± 0.8	300
Hackam [32]	4.0 ± 0.05	6.45 ± 0.1	1.56	294
G.F. Sauter [33]	4.0	—	4.2	335
E.C. Beaty [25]	4.07	6.14	5-7	300
D. Smith [34]	4.6	—	7.9 ± 0.4	295
Bhattacharya [35]	4.0	—	7.7	300
A.P. Vitols [36]	4.0 ± 0.1	—	4.4 ± 0.4	300
Orient [37]	4.13 ± 0.04	6.20 ± 0.07	4.6 ± 0.35	300
R. Johnsen [38]	—	—	6.4 ± 1.2	304-326
This work	4.4	6.2	5.6 ± 0.1	300

2.3.2 Nitrogen

We have measured the reduced mobility of the nitrogen, N_4^+, ion in N_2, under different pressures (6 to 16 Torr) and different reduced electric fields (15 to 35 Td) at 298 K [23]. The extrapolated value to zero field is 2.37 ± 0.02 $cm^2V^{-1}s^{-1}$.

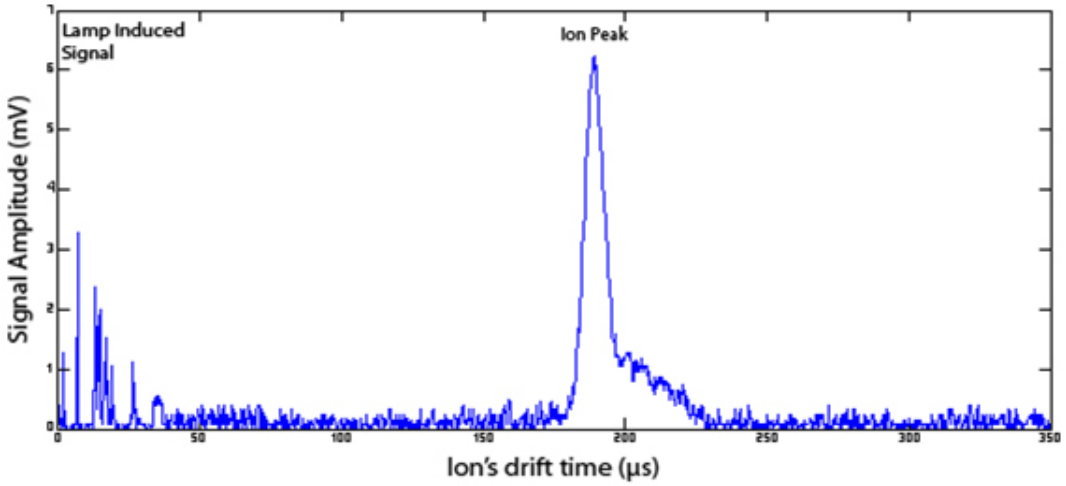

Figure 2.5

Average of 128 digitalized pulses recorded in N_2 at a pressure of 8 Torr, temperature of 24.5 °C for a reduced electric field of 35 Td and for a V_{GEM} of 22V. The signal induced by the UV flash lamp circuitry has been already subtracted but it is still possible to see its remaining contribution on the left hand side of the figure

In the above figure (2.5) it is possible to see a typical pulse from the nitrogen ion. Table 2.3 below, contains the results obtained for the reduced ion mobility under different reduced electric field. Figure 2.6, depicts those results and other author's results.

Table 2.3

N_4^+ reduced mobilities in N_2 at 298 K

E/N (Td)	**K_0 (cm^2 V^{-1} s^{-1})**
15.0 ± 0.06	2.38 ± 0.02
17.5 ± 0.15	2.38 ± 0.01
20.0 ± 0.18	2.37 ± 0.01
22.5 ± 0.31	2.36 ± 0.01
25.0 ± 0.09	2.36 ± 0.01
27.5 ± 0.13	2.37 ± 0.02
30.0 ± 0.20	2.36 ± 0.01
32.5 ± 0.17	2.37 ± 0.03
35.0 ± 0.14	2.36 ± 0.01

Opposite to what happened with neon, the nitrogen data show only one peak, as seen in Figure 2.5. The problem was to identify it, as this experimental apparatus does not provide a direct identification of the ions present in the vessel. Although we could not identify the ion directly, the experimental technique that allows us to control the maximum energy acquired by the photoelectrons inside the GEM holes (as mentioned in section 2.2.1). That proves to be essential to reduce the number of candidates.

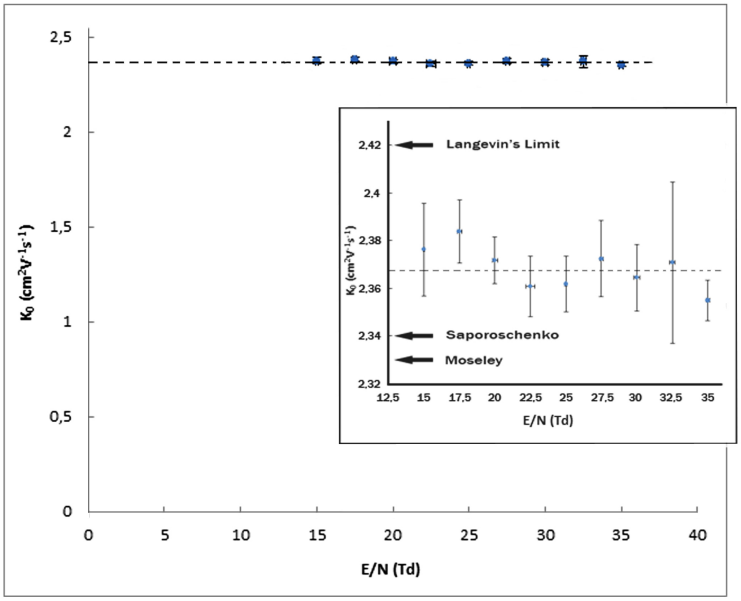

Figure 2.6

Reduced mobility of the produced in N_2 for pressures between 6 and 16 Torr

When comparing our results with those from different authors, we suspected that the ion present should be the N_4^+ ion. This would be later confirmed by a few considerations explained in the next section. Another observation made was that a small lump on the right side of the peak was present. This lump is, most likely, caused by impurities, which we suspect result mostly from outgassing such as H_2O molecules. After evacuating and filling with the active gas a few times we were able to reduce the influence of these impurities to a point where they have a negligible effect on the mobility results. As was said before, not only could we see that this lump reduces after the stated procedure as its ratio to the peak also diminishes. When making the data analysis we made sure the peak was symmetrical so that it could be fitted by a Gaussian. The small lump mentioned must be neglected in order to adjust the peak to a Gaussian. Moreover, in the spectra acquired, the small peaks near the origin are due to the interference of the lamp circuitry.

Ion Identification

As said above the ion was identified as being the N_4^+. We reach this conclusion after few considerations. Firstly, the Langevin limit for this ion was calculated considering that $\alpha = 1.76\,\text{Å}^3$ [21] obtaining the value $2.42\,\text{cm}^2\text{V}^{-1}\text{s}^{-1}$ which is close to our experimental values (just a 2% difference). However, having a value consistent with the Langevin's theory is not enough to confirm the identification of the ion. Thus, more evidence must be attained and when comparing the values in Table 2.4 bellow, it is possible to see that the values we obtained are in good agreement with others authors' work for N_4^+.

Even though this is still not enough to prove that we are observing the referred ion, it is a more accurate hint, since the comparison values used in the table above are taken from

Table 2.4

Values of the zero field mobilities of N_4^+ ions in N_2

Reference	$\mathbf{K_0(cm^2V^{-1}s^{-1})}$	**T (K)**
Saporoschenko [39]	2.34	303 ± 2
J.T. Moseley [40]	2.33 ± 0.08	300
This work	2.37 ± 0.02	298 ± 1.5

experimental works that use direct ion identification processes.

Doubts could still exist, but our last consideration together with the previous ones, leave little or no room at all for other possibilities. If one pays attention to the Table 2.5, where we present the values of the appearance potential for the relevant nitrogen ions in N_2, it is possible to observe that below 21 eV only the N_2^+ and the N_4^+ ions can be formed.

Table 2.5

Values of the appearance potential for N^+, N_2^+, N_3^+ and N_4^+ formation in $N2$

Reference	$\mathbf{N^+}$	$\mathbf{N_2^+}$	$\mathbf{N_3^+}$	$\mathbf{N_4^+}$
Saporoschenko [39]	24.2 ± 0.4	15.5 ± 0.2	22.1 ± 0.5	
G.E. Keller[41]	24.3	15.58	21.5	
R.K. Asundi[42]	24.3 ± 0.1	15.6	21.1 ± 0.1	15.1 ± 0.1

Using the method we have stated in the introduction to this chapter, we control the energy acquired by the ions to a point where only these two ions can be created. However N_2^+ quickly reacts with N_2 forming N_4^+ through the reaction:

$$N_2^+ + 2N_2 \rightarrow N_4^+ + N_2 + 0.87eV \tag{2.13}$$

This reaction rate constant is $\sim 5 \times 10^{-29}$ cm^{6}s^{-1} for fields up to about 40 Td [43, 44, 45] and as the dissociation energy of N_4^+ (0.87eV) is much larger than the kinetic energy of the ion under the low reduced electric field used, the N_4^+ ion once formed will not dissociate back into N_2^+ and N_2. To further support this discussion the results in [46] point out towards the abundance of N_4^+ ions (and residues of other ions species) at E/N values below 100 Td.

Summing up, the reasons that led us to the conclusion that the ion we are observing is the N_4^+ ion are:

a) The experimental reduced mobility value by us attained is about 2 % lower than the value predicted by the Langevin's limit;

b) The reduced mobility value attained by other authors for this same ion is in good agreement with our results;

c) From the only two ions that can be produced with the V_{GEM} we have applied, we only have N_4^+ ions present, since the N_2^+ quickly forms N_4^+ in a non-reversible reaction.

For these reasons we state that the only ion observed is N_4^+.

2.3.3 Xenon-Nitrogen Mixture

Pure xenon mobility studies were already made using this chamber by P.N.B Neves [18]. It is possible to observe in the cited work, that for E/N values below 29 Td there is only one type of ion present in pure xenon: the Xe_2^+ ion. For that reason, the study performed with this mixture was done below 29 Td.

The typical signal induced from the ion Xe_2^+ in Xe-N_2 mixture is depicted bellow. In the figure it is possible to observe that only one ion is present in the mixture.

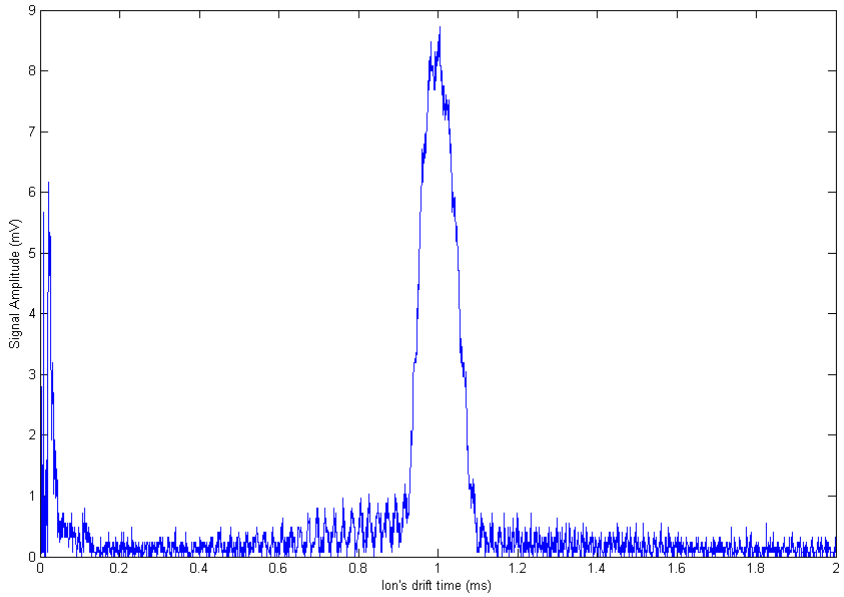

Figure 2.7
Average of 128 digitalized pulses recorded in 95Xe-5N_2 at a pressure of 8 Torr, temperature of 18.5^{o}C for a reduced electric field of 24.6 Td and for a V_{GEM} of 17V.

The graph below depicts the mobility for experimental data acquired for percentages of xenon from 89% to 100%, in the Xe-N_2 mixture, at 24.6 Td and measured for pressures of 4 and 8 Torr.

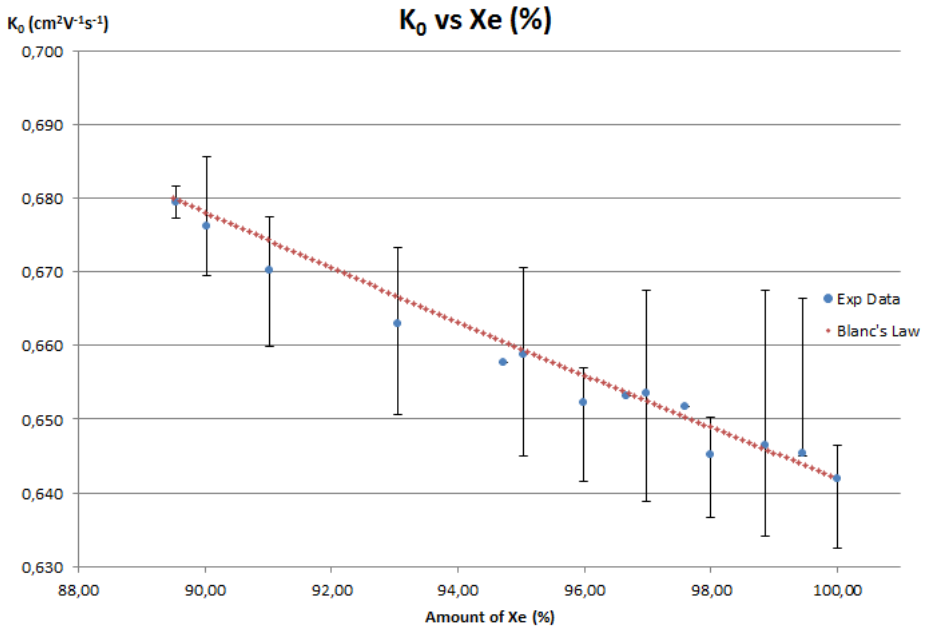

Figure 2.8

Xe-N_2 ion mobility variation vs xenon ratio in the mixture
Data taken for E/N 24.6 Td and pressures of 4 and 8 Torr
Circular pattern are experimental data and diamond pattern the prediction according to Blanc's law

Table 2.6

Comparison of the mobility found experimentally and the mobility expected with Blanc's law theory

Xe(%)	$\mathbf{K_0}$	$\mathbf{K_{0Blanc}}$	**Error (%)**
89.55	0.679	0.680	0.06
90.04	0.676	0.678	0.27
91.02	0.670	0.674	0.60
93.05	0.663	0.667	0.57
94.71	0.658	0.661	0.44
95.04	0.659	0.659	0.09
95.98	0.652	0.656	0.57
96.66	0.653	0.654	0.06
96.98	0.654	0.652	0.16
97.60	0.652	0.650	0.21
97.99	0.645	0.649	0.59
98.87	0.646	0.646	0.08
99.45	0.645	0.644	0.22
100.00	0.642	NA	NA

To calculate Blanc's theory predicted values for the Xe_2^+ ion in N2, we have used the

Langevin's limit formula. Thus, for Xe_2^+ ion in N_2 medium, the value obtained was 1.3719 $cm^2V^{-1}s^{-1}$ calculated using $\alpha = 4.044 Å^3$ taken from [21]. For Xe_2^+ ion in pure Xe, the value used was 0.642 $cm^2V^{-1}s^{-1}$, obtained experimentally, which is somewhat lower than the value in [18]. It is still in good agreement with that value since the difference between both is lower than 1.6%.

The results obtained show clear evidence that adding nitrogen to xenon increases the xenon ions drift velocity. However, data is not enough to assert that this mixture obeys to Blanc's law. A higher statistic is needed to understand if the results obtained are reproducible over a rather high number of measurements. For that reason, and as statistics is not high enough, more measurements are needed to decrease the statistical error.

For the 90Xe-10N_2 mixture there is an increase of 5.8% in the mobility value when compared with the mobility of the ion in pure xenon.

In order to have solid results more data must be taken. It must also be taken data for E/N values over 30 Td. For E/N values of this order of magnitude, in pure xenon there are two ions present [18]. For that reason it is important to evaluate the influence of nitrogen in the mobility of both xenon ions in the N_2-Xe mixture. It is also essential to acquire data for percentages of Xe lower than 90%, so the validity of Blanc's law for this binary mixture can be confirmed or excluded.

It was impossible to acquire more data concerning these measurements due to technical problems that came up in the process (high room temperature).

2.4 IDC Conclusions

2.4.1 Neon

The experimental setup used with neon provided us results for the mobility of Ne^+ ions in Ne under different pressures and reduced electric fields. We identified two ions Ne^+ and Ne_2^+ obtaining the following values, respectively, for their reduced mobilities: 4.4 $cm^2V^{-1}s^{-1}$ and 6.2 $cm^2V^{-1}s^{-1}$. Both values are in good agreement with most of the published data and the dimer ion's reduced mobility is also in good agreement with the Langevin's limit. Finally, we also measured the rate constant of the reaction that converts the atomic ions to dimer ions $Ne^+ + 2Ne \rightarrow Ne_2^+ + Ne$ and obtained a value of $5.6 \pm 0.1\ 10^{32}$ cm^6s^{-1} which is in agreement with other authors' published values in scientific literature.

2.4.2 Nitrogen

We conducted ions mobility measurements of N_2 ions produced in N_2 under different pressure and reduced electric fields. It was possible to identify the only observable ion (N_4^+) and its reduced mobility was measured, for different pressures and reduced electric fields, and a value of 2.37 $\pm$ 0.02 $cm^2V^{-1}s^{-1}$ obtained. These results are in very good agreement (within 1.7%) with those from other authors using different techniques.

2.4.3 Xenon-Nitrogen Mixture

Measurements with xenon-nitrogen mixtures were made, in order to evaluate how the presence of nitrogen influences the mobility of xenon ions. It was possible to conclude that the presence of nitrogen increases the mobility of xenon ions. However, it was not possible to ensure if Blanc's law applies to this mixture, despite the good agreement between the experimental data and the theoretical expected values. Moreover, for NEXT experiment, the important conclusion is that there is a clear trend showing that increasing the presence of nitrogen in xenon will increase xenon ions mobility. It was possible to observe, that adding 10% of nitrogen to xenon increases xenon ion mobility in roughly 6%.

More data must be taken in order to consolidate the results presented here and to confirm or dismiss the validity of Blanc's law.

Chapter 3

NEXT-0

This part of the thesis addresses a contribution to the design and development of the first TPC prototype of NEXT, so-called NEXT-0. The reason for optimizing NEXT-0 is that this first prototype does not work as desired: it has been designed to withstand HVs up to 20 kV in the cathode and pressures up to 10 bar - as for high pressures voltages of more than 10 kV are required to produce electroluminescence light. However, during the operation of the detector, limitations in the HV rating were observed limiting its use to low HVs. Despite the limitations, the detector was used at atmospheric pressures for measuring the response of SiPMs coated with a wavelength shifter and for preliminary energy resolution studies with a PMT, contributing in that way for the NEXT.

The purpose of this part of the work is to improve the performance of NEXT-0 for its future use and to start acquiring data for energy resolution comparison at different pressures and for variable electroluminescence and drift electric fields (E_L and ED). As a value of reference, for this type of detectors about 8% is considered a good energy resolution for 5.9keV x-rays at atmospheric pressure [10], the same source used in this work.

3.1 Introduction

NEXT-0 chamber is basically a Gas Proportional Scintillation Counter (GPSC). It is a first approach to the NEXT TPC, since the Physical principles involved are the same.

A GPSC is based on the principle that the X-radiation interacting in the gaseous detector will produce an output signal proportional to the energy of the incident particle, using electroluminescence as signal amplification (instead the high fluctuation of charge multiplication) [10].

In more detail, and using the example of an X-radiation emitting source, each X-ray photon will interact with the high-pressure gas. This interaction will result in a photoelectron by means of photoionization. The excited ion will decay resulting in other high-energy electrons. The high-energy electrons will lose energy by ionizing and exciting the atoms of the medium. These interactions will produce more electrons and primary scintillation light. In this first stage, where

the electrons will be thermalized, there is a week electric field applied, which drives the electrons towards a second stage where another electric field is applied.

In the second stage, the electric field applied is intense enough so that the electrons colliding with the xenon atoms will gain enough energy to excite (but not to ionize) them. Thus, the only energy-loss interaction type will be atomic excitation by means of which, at the working pressures, molecular excimers are formed. These excimers produce electroluminescence through de-excitation - the already mentioned Secondary scintillation. Part of this electroluminescence will reach and be collected by the PMT that converts it in an electric signal, proportional to the energy of the incident particle, as said before.

As mentioned in the first chapter (section 1.2.1), the Secondary scintillation in xenon is due to the de-excitation of a xenon excited molecule. As mentioned before in equation 1.2, above a few hundred Torr the process is the following:

$$\begin{aligned} Xe^* + 2Xe &\rightarrow Xe_2^{**} + Xe \\ Xe_2^{**} + Xe &\rightarrow Xe_2^{*} + Xe \\ Xe_2^{*} &\rightarrow Xe + Xe + h\nu \end{aligned} \tag{3.1}$$

3.2 Characterization of the Experimental System

A GPSC is based on a scintillation emitting medium whose light is collected in a device, usually a Photo Multiplier Tube (PMT). As in a standard GPSC, in NEXT-0 there are two different regions: A first region, with an electric drift field applied, where the radioactive particles are absorbed, electrons produced and guided towards the next region, where electroluminescence is produced. The electric fields in these two regions have well defined boundaries, which depend on the filling medium and working pressure. The electric field applied to the first stage must not allow the electron to undergo inelastic collisions, whereas in the second stage it must allow the electron to gain enough energy to excite the xenon atoms, but not to ionize them.

3.2.1 Experimental Setup

The experimental system has a main vessel that is connected to the gas circulation system. The gas is purified by means of hot getters. In the main vessel a Teflon cassette is placed vertically and inside holds two metallic pieces set at high voltages. Those are what are called here *anode* and *cathode* or *grids*. The cathode and anode, along with the ground mesh, are responsible for creating the drift and electroluminescence fields. In the figure 3.1 it is depicted the schematic drawing of the main vessel and the parts inside it (final setup).

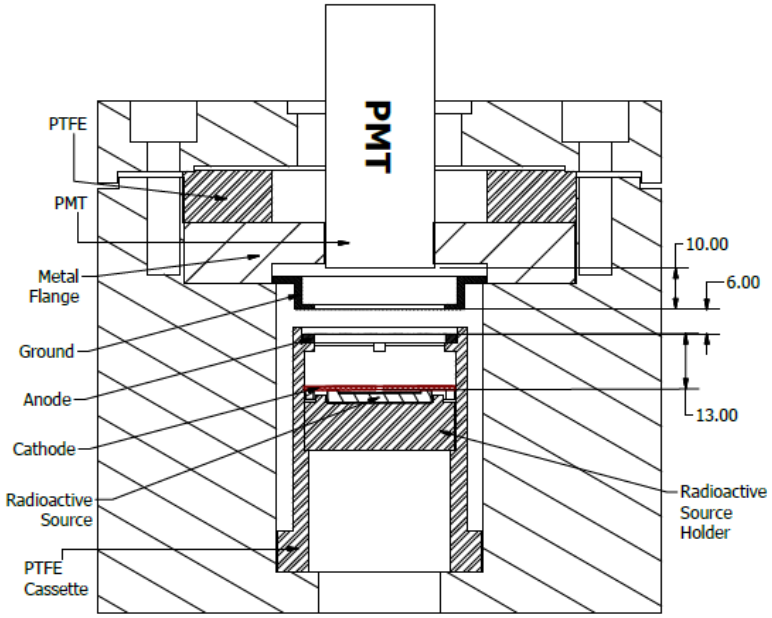

Figure 3.1

Schematic drawing of NEXT-0 chamber

In the figure above it is possible to see that a PMT is placed over a mesh that is located just a few millimetres below it. That mesh is in direct contact with the main vessel and at ground voltage. This mesh is called *Ground*. Below the ground mesh it is placed the anode and further down the cathode. The cathode is placed over the collimated radioactive source (collimator has 1 mm diameter); all these pieces seat on a Teflon support that fits inside the cassette.

In order to acquire data, the system is evacuated, and then filled with gas at the desired pressure. It is then left at rest for a while, allowing the hot getters to purify the gas. Finally, the appropriate high voltages are applied to the cathode and anode establishing the desired electric fields. The data are acquired using a digital oscilloscope directly connected to the PMT.

This digital oscilloscope is set for area calculation, which is equivalent to the integral of the signal over time. This is directly related to the electric signal formed within the PMT, which in its turn is directly related to the amount of light collected.

For this work, the data analysis was performed with ROOT framework [47].

Working Conditions

In the final configuration, the best vacuum pressure attained with this system was of the order of 2.5×10^{-6} mbar and the maximum pressure tested was 5.5 bar (with Argon). The drift field is established between the cathode and the anode (13 ± 0.5 mm apart), and the electroluminescence field is set between anode and ground mesh (6 ± 0.3 mm apart). The strongest stable electroluminescence field reached was of about $3.75\,\mathrm{kVcm^{-1}bar^{-1}}$ at 1.20 bar.

In this system, when increasing the pressure, limitations in the electroluminescence fields

start to appear. It is difficult to reach the $3\,\mathrm{kVcm^{-1}bar^{-1}}$ threshold at pressures above 1.75 bar.

3.2.2 Design limitations & Improvements

As expected from any first prototype, this experimental system has design faults. The most evident ones, the ones that induce limitations to the experimental work, are going to be described in this section. After detecting the most relevant problems, it was possible to fix or minimize some of them. Some parts could stand further improvements, but, for some reason, they were not improved to the limit. In this section are also going to be mentioned improvements made and possible further improvements.

As a reference NEXT-0 was designed to withstand pressures up to 10 bar, with the voltage feedtroughs standing up to 20 kV.

General Considerations

Initially NEXT-0 was meant to work with cold getters and with a recirculation pump. However, at the moment this work was being developed, this system was not implemented and hot getters were in use. For that reason, shorter and thinner pipes would be better when relying on convection to maintain the gas flow. The vessel could be set up in a way that the gas circulation would be easier.

After using the system, it is possible to realize that it has also some problems which are not noticeable at first sight. First of all, the diameter of the body of the detector is too small, which makes the access hard. As most of important pieces go inside the vessel, it is hard to operate. However, the worst problem caused by its small diameter is the fact that the detector walls are too close to the Teflon cartridge, which makes this system more prone to discharges.

Although the vacuum system and the vessel diameter present problems, changes in these parts would imply manufacturing a new vessel. As this would not be a practical solution, we tried to use the existing parts and optimize the experimental system. Regarding the vacuum system, even though it was not possible to design and assemble a new system, a gas recovery bottle was re-introduced. It allows minimizing gas waste.

Teflon Cassette

The diameter of the cassette could not be much smaller because it would reduce the active area, which increases the fields non uniformity. It could not be set larger because it is limited by the inner diameter of the chamber. The actual diameter could, therefore not be modified. This fact makes the system more prone to discharges because of the proximity of the cassette to the metallic inner wall of the vessel. Discharges occur since the cassette has holes for gas flow that minimize the insulation properties of the material.

The cassette small diameter and its closeness to the detector walls creates a problem: the

field lines between the anode and cathode are not as uniform as they would be if the distance between both was much shorter than the meshes' diameters. The same applies between anode and ground.

Another problem is that the cassette creates a path for charges between cathode and anode causing discharges. A final relevant problem identified was related to centring the source in the cassette: since the source diameter is smaller than the cassette inner diameter, when trying to place the cassette in the vessel the source moves.

Although the cassette presented several problems, not all were minimized. Concerning the proximity to the detector's walls, one option tested was to cover the cassette with Kapton. This proved to work, but left doubts about gas circulation. For that reason, this idea was abandoned. It was also verified that having the anode ring covered all around by the cassette would prevent discharges. Although discharges would eventually occur anyway, they would be at higher voltages. That could have been an important improvement. As it was not feasible, another solution to increase the electroluminescence field limit had to be found. Diminishing the distance from the anode to the ground mesh seemed the best compromise. To reduce the distance, a support made of plastic screws was built. These screws also allow the gas to flow and prevent the anode from being in direct contact with the inner walls of the cassette, minimizing the charge flow to the cathode.

Another improvement made to minimize discharges, was making grooves in the Teflon walls increasing the charges' path. Finally, concerning the source centring, a plastic holder was designed and built. This holder keeps the source centred and allows gas flow.

Anode

The first version of the anode was a mesh between two copper rings kept tense by means of screws. The high voltage supply wire is inserted between the copper rings. Discharges were seen to occur at the sharpest edges of these rings and screws and the mesh was not tense. Another problem at the anode was its connection to the high voltage power supplly, which is a wire soldered to a feedthrough. This wire must be neither too long (it will cross the electroluminescence region), nor too short (it will not connect to the anode).

In order to minimize the problems a new anode was made. It is a metallic ring with a mesh glued with conductive Epoxy glue. For covering the interface mesh/ring, a layer of non-conductive Epoxy glue was applied to prevent discharges on the sharpest edges of the mesh and the ring. The metallic ring has a hole to insert the wire and another ring is pressed against it so it holds the wire and forces contact between both (ring and wire).

Although this procedure increased the electric field reachable, a solution to allow reaching even higher electric fields should be found, if studies at pressures over 3 bar and with electric fields over 3 $\mathrm{kVcm^{-1}bar^{-1}}$ are required.

Ground

The ground consisted of a metallic mesh, similar to the anode, placed inside a metallic holder in direct contact with the body of the detector.

There were two problems: first, the anode was too far from the ground mesh, which implies applying very high voltages to reach the same electroluminescence field (increasing sparking risks); second, the field lines were not uniform since the metallic holder was at the same potential as the mesh itself, but at different distances.

Ground improvements were done simply by gluing a metallic mesh to the bottom part of the metallic support by means of Epoxy glue (two layers as for the Anode), reducing the distance from anode to ground and discharge probabilities.

Cathode

The cathode consists of a copper plate perforated in order to allow gas flow. The HV connection is similar to that of the anode, but here the wire is soldered to the copper plate.

There are two problems with the cathode. One is that the airflow is not good. The other is that every time it is necessary to remove the cathode or the Teflon cassette from the detector the HV wire must be cut (cathode is soldered). Cutting the wire and soldering it back again not only is not practical as after cutting the wire a few times it becomes too short and it must be replaced. This implies a great amount of work and delays. The other option was to solder the wire to the cathode inside the vessel, which is too risky since it could introduce too many impurities (such as solder) in the system.

Using the same approach used in the anode, the old cathode was glued with conductive Epoxy to a ring similar to the one in anode. That procedure allows the wire to be removed and placed without having to solder it.

External Radiation

One of the main problems detected after acquiring the first sets of data, was that the system was detecting external radiation, not the radiation from the source. After acquiring and analysing data that did not correspond to the expectations, these data were reviewed and compared to other data. What was happening was that the non-desired radiation impaired the distinction of the events from the radioactive source.

In order to shield the detector from spurious radiations a metallic cover was built. It is a box, with the bottom side open, that covers all the detector's active region. It has a layer with 10 mm thickness of Aluminium and another 2 mm internal layer of Steel – glued to the first with Epoxy.

Limitations in the High Voltages

Some of the problems described earlier do not imply limitations of the system. They merely imply wastes (either gas, materials or time). However, some of the problems do introduce limitations in our experimental work. The limitations are mainly not being able to reach the desired electric fields.

Having a small distance between the Teflon cassette and the detector's walls implies that it is more prone to discharges. The solution would be having a larger vessel diameter. That was not feasible. The small diameter of the cartridge implies field distortions, which create unknowns hard to estimate. Nonetheless, ultimately, the cartridge worst problem is the path for charges it creates. This means that charges can travel from anode to cathode, producing voltage breakdowns. It prevents reaching strong drift fields at high pressures (over 2.5 bar it limits the experimental work). Even with the improvements described, this problem was not completely overcome.

Summing up, the only limitations caused by the system design flaws are in the electric fields attainable, as well as the lack of shielding that prevented the detection of the radioactive source signals. The improvements made allow to reach higher electric fields but not as high as desired; the shielding proved to be an efficient solution for eliminating of the undesirable radiation. Everything else described just increases the difficulty in running the system, but does not affect experimental data collection.

3.3 Data Acquisition

3.3.1 Method

In order to acquire data there are a few steps that must be followed. The Teflon cassette and all its parts must be inside the vessel and in place. The system is evacuated, typically to a pressure near 2.50×10^{-6} mbar. After that, the gas is allowed in, until the desired pressure is reached. The pressure is measured by a Swagelok Pressure Transducer – Ultra High Purity kit.

With the desired pressure inside the chamber, the voltage is set in both anode and cathode. To supply those voltages it is used a FUG – HCP DC power supplier. The Hamamatsu R8520-06SEL PMT is the light collector that is set to a biasing voltage of 750 V, powered by a CAEN N470 programmable HV power supply. At this operating voltage, the PMT has a gain of 5×10^5 . Also, its typical quantum efficiency is 30 %.

The PMT is directly connected to a LeCroy WavePro 7 Zi-A Oscilloscope. This oscilloscope allows area calculation of the signal and automatic creation of spectra/histograms. A typical signal acquisition with the oscilloscope is depicted in 3.2. The source used for data acquisition during this work was a ^{55}Fe collimated source and with a chromium filter placed on top. The activity of this source as of 5 of March of 2012 was about 321kBq. In the figure below is possible to see the data acquired in the oscilloscope's persistence mode. The colours show

that the majority of the signals have a similar behaviour. It is also depicted a one signal superimposing the persistence graph.

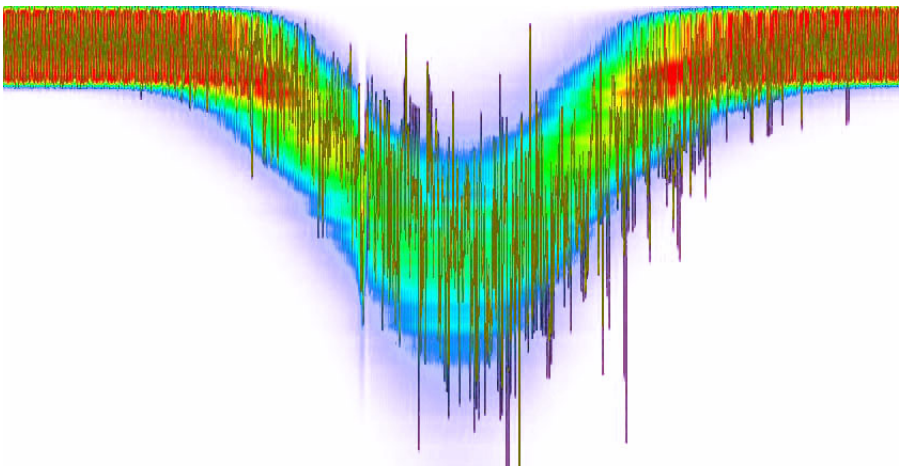

Figure 3.2
Oscilloscope's signal waveform capture. Data taken for several hours in the oscilloscope's persistence mode
Colours illustrate the probability of signal shape
Mean amplitude 40 mV, mean duration 1.5 μs

The charge spectrum is created by integration of the signals in a defined time window of 5ms. The spectrum created by the oscilloscope display the acquired data but no "Zero" level reference. This implies that, after acquiring data, we must set the electric fields to zero and the oscilloscope to auto mode. With this operation the spectrum will include the mean area for the noise, which becomes our reference zero level. In ideal conditions, this value should be zero; however this is never the case. Furthermore, as the source is placed inside the detector, it is not possible to remove the source to acquire data with the same settings in order to obtain the noise contribution.

In the charge data spectra, there are two peaks: the pedestal (noise peak) and the peak from the radioactive source (as it is depicted in 3.3). These two peaks are fitted to Gaussians using ROOT.

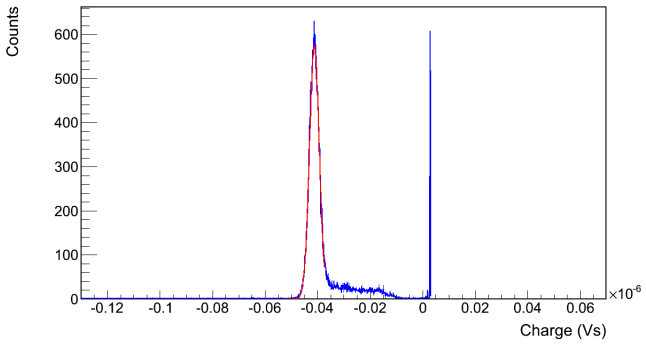

Figure 3.3
Charge spectrum obtained at 1.50bar, $E_L = 3.00\,\mathrm{kVcm^{-1}bar^{-1}}$, $E_D = 0.40\,\mathrm{kVcm^{-1}bar^{-1}}$
The peak on the right is the pedestal and the one on the left is the source peak
The red line is the Gaussian fitting to the data. The resolution obtained was 9.74 %

In order to calculate the energy resolution, as the fitting is a Gaussian fit, we use the equation:

$$FWHM = 2\sqrt{\log 2}\cdot\sigma \tag{3.2}$$

σ value is given by the Gaussian fit. Then the $FWHM$ is divided by the centroid value, given from the difference between the centroid of the source peak and the centroid of the pedestal.

Oscilloscope Settings

As in the oscilloscope charge data spectrum are created according to the signals recorded, there are two oscilloscope settings of major importance: the trigger signal acceptance conditions (width and level) and the integration window.

The trigger width conditions must be large enough to record secondary scintillation only; additionally the level condition should not be too low (it will record all sorts of small signals such as noise signals) or too high (it will only record part of the signal under analysis). Thus the trigger used was set so the oscilloscope records signals that are more negative than $-16.9\,\mathrm{mV}$ and longer than 20 ns. As for the integration window, the oscilloscope does not integrate only the signal, but also the noise around the signal so it should be adjusted. It interferes with the resolution and it should be maintained the same for all data acquisitions. This also stands for the time scale and voltage.

Measurements were performed for pressures of 1.20 bar and 1.50 bar for variable electroluminescence and drift fields 2.5 to 3.75 $\mathrm{kVcm^{-1}bar^{-1}}$ to 0.2 to 0.80 $\mathrm{kVcm^{-1}bar^{-1}}$ respectively.

3.3.2 Energy Resolution vs Pressure

In Figure 3.4 the results obtained for two different pressures are depicted (1.2 and 1.5 bar), at a constant drift field $0.40\,\mathrm{kVcm^{-1}bar^{-1}}$.

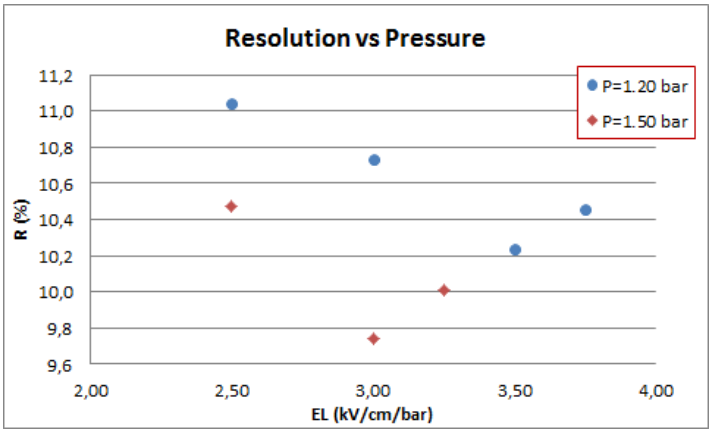

Figure 3.4

Energy resolution as a function of E_L field for pressures of 1.20 and 1.50 bar Constant drift field equal to $0.40\,\mathrm{kVcm^{-1}bar^{-1}}$

Although data is limited, it seems that for similar electroluminescence fields the energy resolution is better at 1.5 bar. It also seems to exist a best energy resolution point, versus E_L plot whose position varies with the pressure: for 1.20 bar at a E_L of $3.50\,\mathrm{kVcm^{-1}bar^{-1}}$ and for the 1.50 bar data, at a E_L of $3.00\,\mathrm{kVcm^{-1}bar^{-1}}$ electroluminescence field. Without further data is hard to conclude if this is the case, but a similar effect has been reported in the literature.

Using the example of [48] for xenon at a pressure of 800 Torr (~ 1.07 bar), the best resolution attained is for $6.00\,\mathrm{kVcm^{-1}bar^{-1}}$, as can be seen in Figure 3.5:

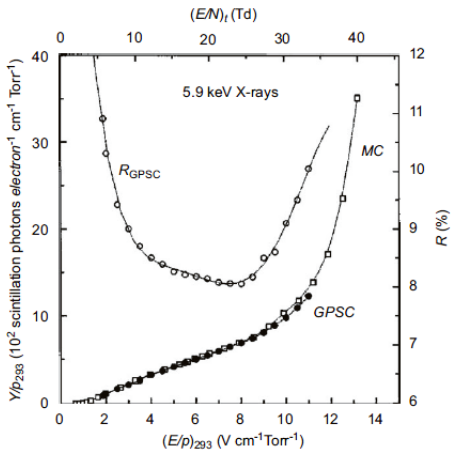

Figure 3.5

Resolution in function of E/P for 800 Torr (~ 1.07 bar) operation pressure (taken from [48])

An effect that is also worth emphasizing is that the apparent "sweet point" for resolution seems to be at lower electroluminescence fields for higher pressure. Using the experimental data present in figure 3.5 adding to what we have seen in NEXT0 it seems plausible to assume so. Once again, only with further measurements at higher pressure would it be possible to confirm

or dismiss these observations.

3.3.3 Energy Resolution vs Drift Field

Figure below depicts the energy resolution attained for measurements performed at 1.20 bar pressure and for different drift fields. Three sets of data are depicted ($3.00, 3.50$ and $3.75\,\mathrm{kVcm^{-1}bar^{-1}}$):

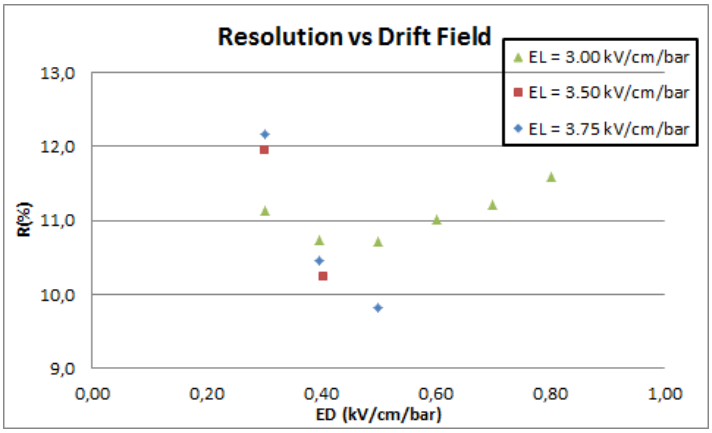

Figure 3.6
Energy resolution in function of drift field for a pressure of 1.20 bar *and different electroluminescence fields*

Regarding the set for which more data was acquired (E_L=$3.00\,\mathrm{kVcm^{-1}bar^{-1}}$), it is possible to observe that, similarly to what was seen for constant E_D at different pressures, there is a best energy resolution point when varying the drift field. In this case, it should be between 0.40 and $0.50\,\mathrm{kVcm^{-1}bar^{-1}}$. For the other two E_L fields not enough data were collected so no conclusions can be drawn.

Although it is not clear, it seems that for stronger electroluminescence field, stronger drift fields must be applied to reach the best energy resolution point

3.3.4 Energy Resolution vs Electroluminescence Field

Figure 3.7 shows the effect of the E_L field on the energy resolution for several drift fields.

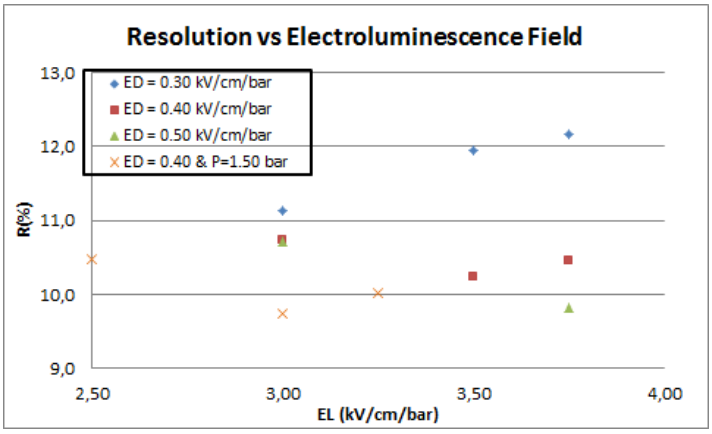

Figure 3.7

Energy resolution in function of electroluminescence field for a pressures of 1.20 and 1.50 bar and different drift fields

The markers that in the legend do not have the pressure are at 1.20 bar

It is possible to observe that for a low E_D fields, the energy resolution becomes worse when the E_L is stronger. For a drift field of $0.50\,\mathrm{kVcm^{-1}bar^{-1}}$, within the electric fields applied increasing the E_L improves the energy resolution. From these data, for pressure of 1.20 bar and $E_D = 0.40\,\mathrm{kVcm^{-1}bar^{-1}}$, it is hard to conclude the trend, but it seems that increasing the E_L over $E_D = 3.50\,\mathrm{kVcm^{-1}bar^{-1}}$ not does not improve the resolution, but actually deteriorates it. The same happens for a drift field of $0.40\,\mathrm{kVcm^{-1}bar^{-1}}$ and pressure of 1.50 bar, that seems to have the best resolution point for $E_L = 3.00\,\mathrm{kVcm^{-1}bar^{-1}}$.

3.4 NEXT-0 Conclusions

Despite the insufficient amount of data taken, it is possible to draw very preliminary conclusions on the dependence of the energy resolution with the E_L and E_D fields. These data suggest that for both electroluminescence and drift electric fields applied, there is an ideal value, beyond which the energy resolution will not improve. Thus, what we can say is that there are hints that the higher pressure the lower the E_L and E_D fields needed for the best energy resolution point to be attained. The observed trends are compatible with existing works reported in the literature [49]. Further measurements should be made in order to draw more thorough conclusions about the effects mentioned.

In addition, to optimize NEXT-0 so it allows to work with pressures up to 10 bar as desired, modifications in the vessel should be made, since the limitations are a consequence of the small diameter of this part.

Chapter 4

Cylindrical Proportional Counter

The idea for this part of the work was to build a Cylindrical Proportional Counter (CPC) to perform experimental measurements with high pressure xenon (pure and mixtures) in order to obtain pulse height spectra and energy resolution data for different settings. The CPC is projected to work simultaneously and in parallel with a GPSC similar to, but simpler than, NEXT-0. The advantage of having these two detectors working together is that it allows cross-checking in the identification of eventual processes such as recombination, attachment, scintillation losses, etc., that may occur at high pressures and more probably in mixtures. The final purpose of these experimental measurements is, once again, to contribute to NEXT by helping to substantiate the choice of a xenon based mixture, evaluating the costs-benefits of possible mixtures.

It is known that some dopants increase Xe drift velocity and diminish diffusion coefficients [17, 50]. However, not all potentially interesting mixtures for NEXT have been fully explored and the effects of recombination and attachment in some particular xenon mixtures that may be interesting are not reported in the literature. Studying recombination effects using a CPC has already been done by [51]. Nonetheless, as it is projected to have the GPSC also working with the CPC, recombination effects and their influence in scintillation yield should also be possible to study. In this way, the experimental apparatus, with the CPC and GPSC, is going to provide means to better understand the behaviour of some dopants on xenon – how they influence recombination, scintillation and energy resolution.

4.1 Introduction

To perform the relevant measurements to study recombination and its effects, there are some Physical concepts that should be present. The most relevant ones are recombination and its effects in luminescence.

Recombination

Recombination is an effect by which an ion re-captures its electron. It is responsible for degrading energy resolution in GPSC as it diminishes the number of available free electrons

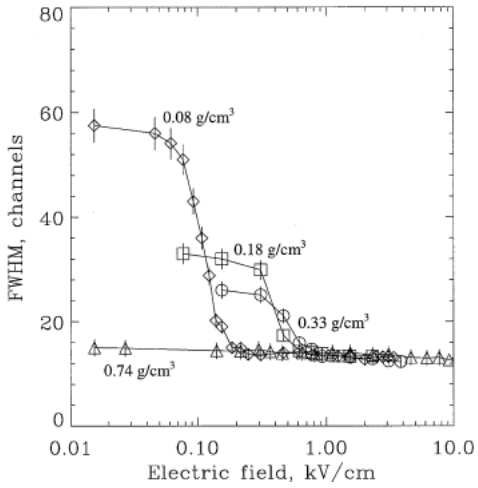

Figure 4.1
Results of a scintillation chamber working with xenon
Depicts the FWHM for different densities varying the electric field applied (taken [52])

In Figure 4.1 we can see that for the data taken at 0.08, 0.18 and $0.33\,\mathrm{g}\cdot\mathrm{cm}^{-3}$ when increasing the electric field the FWHM rapidly improves until it reaches a point that increasing the electric field further does not further affect the FWHM. As discussed in [52], one possible explanation for this effect is related to recombination.

Before going into more details, a few important considerations should be pointed out regarding recombination.

Initial/Geminate Recombination & Volume/Random Recombination

There are are two similar effects but with different origins for recombination occurrence [52].

In a medium where no electric field is applied, an electron produced by an ionizing particle that becomes thermalized near its parent ion has 100% probability of recombining with the parent ion. The phenomenon by which the parent ion re-captures its electron near the initial event area is called Geminate recombination.

However, even at zero field, there is a probability that an electron produced by an ionizing particle only becomes thermalized far away from the parent ion. In that case, the Coulomb force between the parent ion and the electron is negligible compared to the electron energy and the electron may escape from Geminate recombination. In addition, if an electric field is applied in the ionization region, the probability of this type of recombination also decreases; if the electric field is high enough Geminate recombination be negligible.

Thus, if an electron produced by an ionizating particle escapes Geminate recombination, but is hovering near other ions (high ionization density medium) after thermalization, it can still recombine with another ion. This type of recombination, which takes place far away from the initial interaction region, is called Random or Volume recombination. In this case, the recombination probability depends on how long the electron stays in the area of the ions. Applying an electric field can reduce or even entirely overcome this type of recombination.

Scintillation Process

According to [53] there are two major scintillation processes in gaseous xenon: *Excitation Luminescence* and *Recombination Luminescence*. The excitation luminescence (already mentioned and explained in equation 1.2) is due to excited atoms directly produced by charged particles, as follows [10, 53]:

$$\begin{aligned} Xe^* + 2Xe &\rightarrow Xe_2^{**} + Xe \\ Xe_2^{**} + Xe &\rightarrow Xe_2^{*} + Xe \\ Xe_2^{*} &\rightarrow Xe + Xe + h\nu \end{aligned} \tag{4.1}$$

The recombination luminescence process is the following [53]:

$$\begin{aligned} Xe^+ + Xe + Xe &\rightarrow Xe_2^+ + Xe \\ e(E_{hot}) &\rightarrow e(E_{th}) + heat \\ e(E_{th}) + Xe_2^+ &\rightarrow Xe^{**} + Xe \\ Xe^{**} &\rightarrow Xe^* + heat \\ Xe^* + 2Xe &\rightarrow Xe_2^{**} + Xe \\ Xe_2^{**} + Xe &\rightarrow Xe_2^{*} + Xe \\ Xe_2^{*} &\rightarrow Xe + Xe + h\nu \end{aligned} \tag{4.2}$$

Xe^+ is an atomic Xe ion, Xe_2^+ is a molecular Xe ion, $e(E_{hot})$ refers to electrons with a kinetic energy of sub-excitation level (< 8.5 eV), $e(E_{th})$ refers to electrons with thermal kinetic energy (~ 0.04 eV), Xe^{**} is a highly excited Xe atom.

Although both scintillation processes are similar, their origin is different, having different time profiles and responding differently to eventual electric fields applied.

Recombination Effects on Resolution

The intrinsic energy resolution in the NEXT TPC is estimated in [54] as being:

$$\frac{\delta E}{E} = 2.35 \left(\frac{F + G + L + \frac{n^2}{mN_I}}{N_I \varepsilon^2} \right)^{\frac{1}{2}} \tag{4.3}$$

where E is a fixed value for the electrons depositing energy, F is the Fano factor, G is a factor dependent on fluctuations in the detected signal, L is a factor that represents the loss of primary ionization (where $L = 1 - \varepsilon$ and ε the overall electron collection efficiency), n is the electric noise, m is the multiplication factor in gain processes (such as avalanche multiplication), finally N_I is the total number of free electrons.

The recombination processes may have an influence in G and L, which can imply altering the intrinsic resolution. Adding a dopant to xenon will most likely increase F, thus harming the energy resolution. However, the dopant may alter the relation between the many factors in equation 4.3 in such a way that the intrinsic energy resolution improves. As well, the dopants may increase the xenon ions drift velocity without compromising drastically the primary scintillation light.

4.1.1 Proportional Counter Basic Principles

The cylindrical proportional counter is a basic radiation detection device developed in the 1940s [15]. Due to its simplicity and robusteness, it still has an important role in the detection and spectroscopy of low-energy X-rays. As it is a well know type of device and it is well documented in the literature [15, 55, 56] it will not be discussed extensively here. However, a few considerations should be made.

The basic principle of operation is a metallic wire (*Anode*) at a positive HV that crosses a cylinder. The cylinder acts as *Cathode* and is grounded. X-ray particles entering the detector will interact with the gas medium, producing electron-ion pairs. The electrons will be guided by the electric field, which becomes more intense as the electron approaches the anode, since the electric field is proportional to the inverse of radial distance (*1/r*).

When electrons are near the anode (typical 2 or 3 times the anode's diameter), the electric field is intense enough and it will give electrons enough energy to ionize the surrounding particles. Each new electron will produce more electrons, which originates an avalanche effect. In the end, all electrons are collected at the anode. This avalanche is known by *Townsend* avalanche. The electrons produced at each avalanche are collected at the anode and induce an electrical signal that will feed an amplification system. The ions produced will be drifting towards the cathode and, eventually, will re-acquire an electron and become neutral atoms again.

Working with *E/p* in the so called *Proportional Region* guarantees that the signal collected is proportional to the energy of the initial event.

4.2 Experimental Apparatus

The experimental apparatus is simple. There is a CPC and a GPSC in the same gas system, which can be isolated by valves. Hot getters, vacuum pumping system, pressure gauge are common to both systems, but gas can still circulate even if one of the detectors is isolated.

In the CPC, the anode is a gold plated tungsten wire with a diameter of 45 μm, the cathode is

a 2 mm thickness cylindrical tube with internal diameter of 32.20 mm. This cylinder is inserted in a DN standard cross that is the main external body. The cylindrical tube has the purpose of maintaining the electric field uniformity. It is perforated to avoid gas to get trapped between the metallic cross and the tube.

At the centre of the external cross and perpendicular to the anode, there is a window for the radioactive source. The window is a 1 mm hole with a Kapton film glued, by means of epoxy glue. The film has a 40 µm thickness and it was aluminized with a layer of ~ 90 nm.

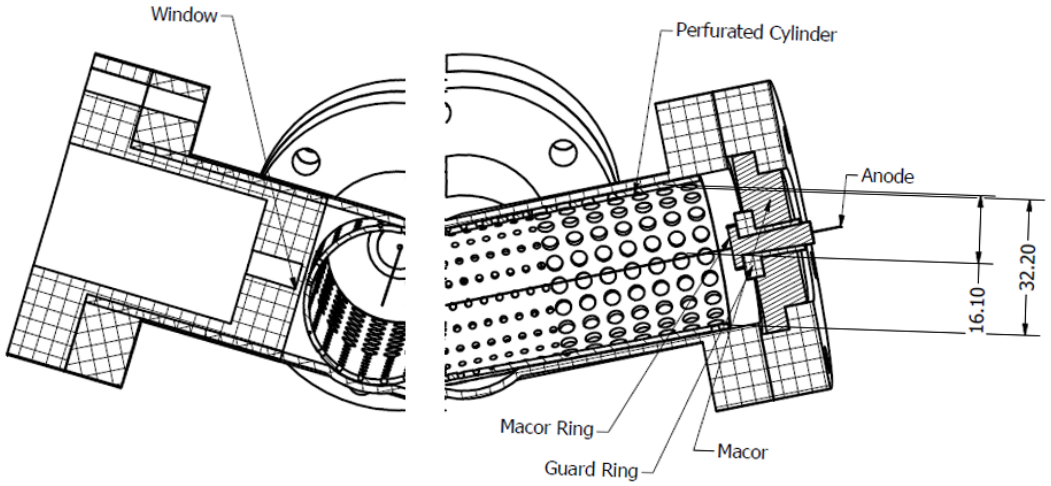

Figure 4.2
Schematic representation of the Cylindrical Proportional Counter
The two different perspectives are perpendicular to each other

The anode is connected to a polarization circuit that also feeds the guard ring. This circuit provides the HV supply and delivers the signal to be amplified to the pre-amplifier Canberra 2006. The signal from the pre-amplifier output is further processed by a Tennelec TC 243 amplifier and to a Ortec Trump PCI 2k MCA. The data taken with the MCA is analysed using ROOT.

In Figure 4.3 a block diagram is illustrating how the experimental apparatus is connected and Figure 4.2 is a schematic representation of the body of the CPC.

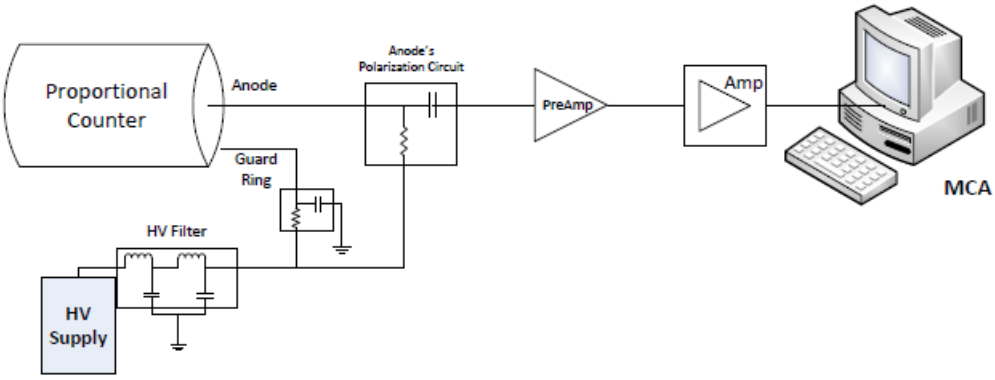

Figure 4.3

Cylindrical Proportional Counter Block Diagram

4.3 Testing Data & Discussion

During these data acquisition the amplifier was set to 20×0.55 amplification, a peaking time of 16 μs and a shaping time of 8 μs.

A testing data spectrum obtained for Xe at 800 Torr is depicted bellow:

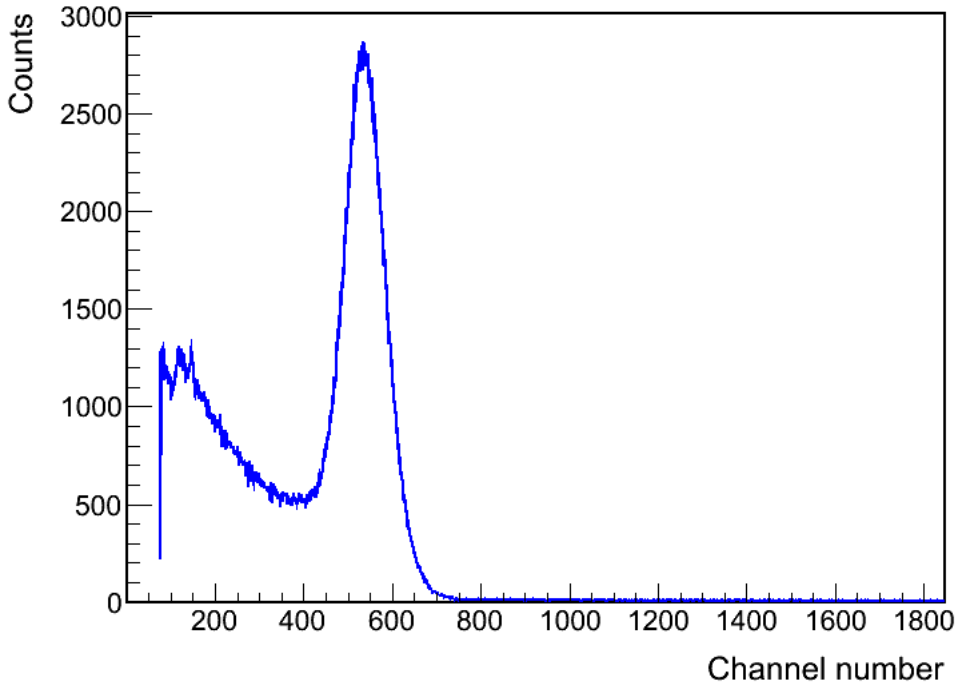

Figure 4.4

Testing data acquisition - pulse height spectra for 800 Torr of Xe and anode at 2kV Lower Level Discriminator set to channel 80

The testing data obtained are the following:

Table 4.1
Testing data obtained for 800 Torr pressure

V (kV)	Dopant	Dopant (%)	Peak (MCA Ch)	FWHM (MCA Ch)
2,00	NA	0,0	350,9	71,6
2,00	Ar	10,0	536,1	116,4
2,00	CH_4	2,5	372,3	77,8
1,90	NA	0,0	140,4	12,7
1,90	Ar	10,0	187,6	17,1

The first thing that must be mentioned is that no data was taken over 800 Torr because distortions in the signal coming from the pre-amplifier would appear. This clear shows a limitation in the experimental setup that must be overcome. Furthermore, even for 800 Torr limitations were visible for pure Xe, as no signal was possible to acquire for voltages in the anode higher than 2.15 kV. Also with 10% Ar and 2.5% CH_4 mixtures not even the 2.10 kV tensions were possible to apply.

In respect to the testing data acquired, it shows that data is already possible to acquire with this CPC.

4.4 CPC Conclusions

The work developed in this chapter was the design, development, assembling and testing of a system consisting in a CPC and a GPSC. The main goal was to build a CPC starting from a constrained geometry (a DN standard metallic cross) suitable to work at pressures above the atmospheric. The CPC was successfully built and assembled as well as the GPSC. Testing showed that both the CPC and the GPSC handle up to 5000 Torr in pressure.

Furthermore, the CPC is operational at 800 Torr. However, testing data shows clear evidence of the limitations for pressures over 1000 Torr, which implies that improvements must be done before usable data can be acquired. After all limitations overcome and the GPSC working the desired works should became possible to perform.

Chapter 5

General Conclusions

The purpose of this Master thesis was to contribute to NEXT by providing more information about xenon based gaseous mixtures.

In Chapter 2, Ne, N_2 and Xe-N_2 ions mobilities were measured. In Ne it was possible to measure the mobility of the atomic and dimer ions with zero field extrapolation values of $4.4\,\mathrm{cm^2V^{-1}s^{-1}}$ and $6.2\,\mathrm{cm^2V^{-1}s^{-1}}$ respectively. The reaction rate of reaction that converts the Ne^+ ions into Ne_2^+ ions was also measured with an average value of $5.6 \pm 0.1 \times 10^{-32}\,\mathrm{cm^6s^{-1}}$.

In N_2 the mobility of the N_4^+ ion was measured for pressures between 6 and 16 Torr and electric field of 15 to 35 Td. The extrapolated value to zero field is $2.37 \pm 0.02\,\mathrm{cm^2V^{-1}s^{-1}}$.

It was also possible to conclude that doping the xenon with nitrogen increase the xenon ions mobility. It was not possible to ensure if this mixture obeys to Blanc's law, but data shows that 10% of N_2 in a xenon medium increases the xenon ions mobility by about 6%. This study lacks more solid evidence, since data taken is insufficient to reduce the statistical error. As technical problems occurred the experimental work had to be put on hold.

In Chapter 3, the objective of improving the NEXT-0 prototype was attained. However, not all limitations were possible to overcome. As it was designed to work up to 10 bar, to improve it to that point the diameter of the vessel must be increased and it was not possible during the work presented here.

Furthermore experimental measurements were possible. The data that was possible to acquire was not as much as desired but it gives hints for additional studies that can be performed with this experimental system. The experimental results suggest that for higher pressures the energy resolution's sweet point is reached at lower electroluminescence fields. Additionally, they suggest that for attaining the same energy resolution, the intenser the electroluminescence field is the intenser the drift field must be.

Finally, in Chapter 4, a Cylindrical Proportional Counter was built to study recombination effects in high pressure xenon (pure and mixtures). The CPC was projected to work simultaneously and in parallel with a Gas Proportional Scintillation Counter, allowing for scintillation studies as well. The CPC is working, however it needs optimization to overcome the limitations.

The GPSC is already assembled and it should be possible to proceed with the planned work soon.

As said before, for the work developed in chapter 3 and 4 data is not as much as desired, as the main objectives were not the results but to have the experimental systems working. The work performed is, in that way, enough to allow us to plan future work. With the Ion Drift Chamber, mixtures of xenon and CH_4, CF_4 and TMAE are going to be studied as well and the Xe-N_2 study completed. NEXT-0 can be used to perform similar and more detailed studies for a wider range of pressure, electroluminescence and drift fields. Similarly, the CPC should allow for studies at pressures between 800 and 5000 Torr, as well as studies for different gas additives in xenon, such as TMAE and CF_4.

Summing up, all main objectives were accomplished, however more data should be taken and more mixtures should be studied. Future work is now planned.

Bibliography

[1] Laboratorio Subterráneo de Canfranc. http://www.lsc-canfranc.es/en/.

[2] J. Díaz *et al.* The NEXT experiment. *Journal of Physics: Conference Series*, 179(1): 012005, 2009. doi: 10.1088/1742-6596/179/1/012005. URL http://dx.doi.org/10.1088/1742-6596/179/1/012005.

[3] N.N. Singh Ng.K. Francis. Validity of quasi-degenerate neutrino mass models and their predictions on baryogenesis. *Nuclear Physics B*, 863(1):19–32, October 2012. doi: 10.1016/j.nuclphysb.2012.05.017. URL http://dx.doi.org/10.1016/j.nuclphysb.2012.05.017.

[4] The NEXT Collaboration. Letter of Intent to the LSC Scientific Committee - NEXT, a HPGXe TPC for neutrinoless double beta decay searches, July 2009.

[5] The NEXT Collaboration. NEXT-100 Technical Design Report (TDR). Executive summary. Technical report, The NEXT Collaboration, June 2012. URL http://dx.doi.org/10.1088/1748-0221/7/06/T06001.

[6] Petr Vogel Steven R. Elliott. Double beta decay. *Annual Review of Nuclear and Particle Science*, 52:115–151, December 2002. doi: 10.1146/annurev.nucl.52.050102.090641. URL http://dx.doi.org/10.1146/annurev.nucl.52.050102.090641.

[7] David Nygren. Optimal detectors for WIMP and $0-\nu\beta\beta$ searches: Identical high-pressure xenon gas TPCs? *Nuclear Instruments & Methods in Physics Research A*, 581(3):632–642, July 2007. doi: 10.1016/j.nima.2007.07.062. URL http://dx.doi.org/10.1016/j.nima.2007.07.062.

[8] J.J. Gómez-Cadenas *et al.* Sense and sensitivity of double beta decay experiments. *Journal of Cosmology and Astroparticle Physics*, 2011, June 2011. doi: 10.1088/1475-7516/2011/06/007. URL http://dx.doi.org/10.1088/1475-7516/2011/06/007.

[9] A. Gando *et al.* Measurement of the double-β decay half-life of 136Xe with the KamLAND-Zen experiment. *Physical Review C*, 85(4):045504, Apr 2012. doi: 10.1103/PhysRevC.85.045504. URL http://dx.doi.org/10.1103/PhysRevC.85.045504.

[10] C.A.N. Conde. *Gas Proportional Scintillation Counters for X-ray Spectometry.* John Wiley and Sons LTD, England, 2004.

[11] I.K. Bronic. On a relation between the W value and the Fano facotr. *Journal of Physics B: Atomic, Molecular and Optical Physics*, 25(8):L215–L218, April 1992. doi: 10.1088/0953-4075/25/8/004. URL http://dx.doi.org/10.1088/0953-4075/25/8/004.

[12] F.P. Santos *et al.* Monte Carlo simulation study of the Fano factor, w value, and energy resolution for the absorption of soft x rays in xenon–neon gas mixtures. *Journal of Applied Physics*, 89(12):8202–8213, June 2001. doi: 10.1063/1.1371281. URL http://dx.doi.org/10.1063/1.1371281.

[13] S.J.C. do Carmo *et al.* Experimental Study of the ω-Values and Fano Factors of Gaseous Xenon and Ar-Xe Mixtures for X-Rays. *IEEE Transactions on Nuclear Science*, 55(5):2637–2642, October 2008. doi: 10.1109/TNS.2008.2003075. URL http://dx.doi.org/10.1109/TNS.2008.2003075.

[14] Maria Filomena de Osório Pinto dos Santos. *Detectores Gasos para Raios: Simulação e Estudo Experimental*. PhD thesis, Universidade de Coimbra - Faculdade de Ciências e Tecnologia, Coimbra, 1994.

[15] Glenn F. Knoll. *Radiation Detection and Measurement*. John Wiley & Sons, Inc, Third edition, 2000.

[16] P.N.B. Neves *et al.* Experimental measurement of the mobilities of atomic and dimer Ar, Kr, and Xe ions in their parent gases. *Journal of Chemical Physics*, 133(124316), September 2010. doi: 10.1063/1.3497651. URL http://dx.doi.org/10.1063/1.3497651.

[17] David Nygren. High-pressure xenon gas electroluminescent TPC fo $0-\nu\beta\beta$-decay search. *Nuclear Instruments and Methods in Physics Research A*, 603(3):337–348, May 2009. doi: 10.1016/j.nima.2009.01.222. URL http://dx.doi.org/10.1016/j.nima.2009.01.222.

[18] P.N.B. Neves. *Studies on the mobility of monoatomic and dimer noble gas ions in their parent gases*. PhD thesis, Universidade de Coimbra - Departamento de Física, Coimbra, 2009.

[19] P.N.B. Neves *et al.* Experimental Measurement of the Ne^+ and $Ne2^+$ Mobilities in Ne and the Reaction Rate Coefficient for $Ne^+ + 2Ne \rightarrow Ne_2^+ + Ne$. *IEEE Transactions on Nuclear Science*, 58(4):2060–2063, August 2011. doi: 10.1109/TNS.2011.2158849. URL http://dx.doi.org/10.1109/TNS.2011.2158849.

[20] P.N.B. Neves *et al.* Measuring the mobilities of the ions formed in P-10 mixtures. *IEEE Nuclear Science Symposium Conference Record*, pages 717–719, 2009.

[21] E.A. Mason H.E. Revercomb. Theory of Plasma Chromatography/Gaseous Electrophoresis - A Review. *Analytical Chemistry*, 47(7):970–983, June 1975. doi: 10.1021/ac60357a043. URL http://dx.doi.org/10.1021/ac60357a043.

[22] L.M. Chanin M.A. Biondi. Blanc's Law-Ion Mobilities in Helium-Neon Mixtures. *Physical Review*, 122(3):843–847, May 1961. doi: 10.1103/PhysRev.122.843. URL http://dx.doi.org/10.1103/PhysRev.122.843.

[23] A.N.C. Garcia *et al.* A new contribution to the experimental measurement of the N_4^+ ion mobility in N_2 at 298K. *Journal Of Instrumentation*, 7(P02012), February 2012. URL http://stacks.iop.org/1748-0221/7/i=02/a=P02012.

[24] Earl W. McDaniel Edward A. Mason. *Transport Properties of Ions in Gases*. John Wiley & Sons, Inc, New York, 1988. doi: 10.1002/3527602852. URL http://dx.doi.org/10.1002/3527602852.

[25] P.L. Patterson E.C. Beaty. Mobilities and reaction rates of neon ions in neon. *Physical Review*, 170(1):116–121, June 1968.

[26] John A. Hornbeck. The Drift Velocities of Molecular and Atomic Ions in Helium, Neon, and Argon. *Physical Review Second Series*, 84(4):615–610, November 1951. doi: 10.1103/PhysRev.84.615. URL http://dx.doi.org/10.1103/PhysRev.84.615.

[27] L.M. Chanin M.A. Biondi. Mobilities of Atomic and Molecular Ions in the Noble Gases. *Physical Review*, 94(4):910–916, May 1954. doi: 10.1103/PhysRev.94.910. URL http://dx.doi.org/10.1103/PhysRev.94.910.

[28] M.A. Biondi L.M. Chanin. Temperature Dependence of Ion Mobilities in Helium, Neon, and Argon. *Phys. Rev.*, 106:473–479, May 1957. doi: 10.1103/PhysRev.106.473. URL http://dx.doi.org/10.1103/PhysRev.106.473.

[29] J.J. Lennon M.J. Mulcahy. Ambipolar Diffusion Measurements in Low Pressure Rare Gas Afterglows. *Proceedings of the Physical Society*, 80(3):626, 1962. doi: 10.1088/0370-1328/80/3/307. URL http://dx.doi.org/10.1088/0370-1328/80/3/307.

[30] V.R. Mittelstadt H.J. Oskam. Ion Mobilities in Helium, Neon, and Argon. *Phys. Rev.*, 132:1435–1444, Nov 1963. doi: 10.1103/PhysRev.132.1435. URL http://dx.doi.org/10.1103/PhysRev.132.1435.

[31] P.L. Patterson E.C. Beaty. *Proceedings of the Sixth International Conference on Ionization Phenomena in Gases*, 1:289, 1968.

[32] R. Hackam. Temperature variation of positive ion mobilities and conversion rates in neon. *British Journal of Applied Physics*, 17(2):197, 1966. doi: 10.1103/PhysRevC.85.045504. URL http://dx.doi.org/0508-3443/17/i=2/a=307.

[33] G.F. Sauter *et al.* Studies of decaying plasmas produced in neon and helium-neon mixtures. *Physica*, 32(11-12):1921 – 1937, 1966. doi: 10.1016/0031-8914(66)90158-3. URL http://dx.doi.org/10.1016/0031-8914(66)90158-3.

[34] P.R. Cromey D. Smith. Conversion rates and ion mobilities in pure neon and argon afterglow plasmas. *Journal of Physics B: Atomic and Molecular Physics*, 1(4):638–649, June 1968. doi: 10.1063/1.1371281. URL http://dx.doi.org/10.1063/1.1371281.

[35] A.K. Bhattacharya. Mass Spectrometric Study of Neon Afterglow Plasmas. *Journal of Applied Physics*, 42(11):4216–4220, 1971. doi: 10.1063/1.1659756. URL http://link.aip.org/link/?JAP/42/4216/1.

[36] H.J. Oskam A.P. Vitols. Reaction Rate Constant for $Ne^+ + 2Ne \rightarrow Ne_2^+ + Ne$. *Physical Review A*, 5:2618–2622, June 1972. doi: 10.1103/PhysRevA.5.2618. URL http://link.aps.org/doi/10.1103/PhysRevA.5.2618.

[37] O.J. Orient. Mobility of mass-identified ions in neon and reaction-rate coefficient for $Ne^+ + 2Ne \rightarrow Ne_2^+ + Ne$. *Chemical Physics Letters*, 23(4):579–581, 1973. doi: 10.1016/0009-2614(73)89033-5. URL http://dx.doi.org/10.1016/0009-2614(73)89033-5.

[38] M.A. Biondi R. Johnsen, A. Chen. 3-body association reactions of He^+, Ne^+, and Ar^+ ions in their parent gases from 78K to 300K. *Journal of Chemical Physics*, 73(4):1717–1720, 1980. doi: 10.1063/1.440307. URL http://dx.doi.org/10.1063/1.440307.

[39] M. Saporoschenko. Mobility of Mass-Analyzed N^+, N_2^+, N_3^+, and N_4^+ Ions in Nitrogen Gas. *Physical Review*, 139(2A):A352–A356, February 1965. doi: 10.1103/PhysRev.139.A352. URL http://dx.doi.org/10.1103/PhysRev.139.A352.

[40] J.T. Moseley *et al.* Mobilities, Diffusion Coefficients, and Reaction Rates of Mass-Indentified Nitrogen Ions in Nitrogen. *Physical Review*, 178(1):240–248, February 1969. doi: 10.1103/PhysRev.178.240. URL http://dx.doi.org/10.1103/PhysRev.178.240.

[41] G.E. Keller *et al.* General Considerations Concerning Apparent Mobilities in Mixed Ion Populations: Drift Velocities of Mass-Identified N^+, N_2^+, N_3^+, and N_4^+ Ions in Nitrogen. *Physical Review*, 140(5A):A1535–A1546, June 1965. doi: 10.1103/PhysRev.140.A1535. URL http://dx.doi.org/10.1103/PhysRev.140.A1535.

[42] R.K. Asundi *et al.* Studies of N_4^+ and N_3^+ ion formation in nitrogen using high-pressure mass spectrometry. *Journal of Chemical Physics*, 47(5):1584–1591, February 1967. doi: 10.1063/1.1712137. URL http://dx.doi.org/10.1063/1.1712137.

[43] Alexandre Bekstein. *Donnees de base des ions polyatomiques dans les gaz d'echappement : modelisation et validation experimentale.* PhD thesis, Université Toulouse III - Paul Sabatier, 2009.

[44] P.A.M. van Koppen *et al.* lon-molecule association reactions: A study of the temperature dependence of the reaction $N_2^+ + N_2 + M \rightarrow N_4^+ + M$ for $M = N_2$, Ne, and He: Experiment and theory. *Journal of Chemical Physics*, 81(1):288–297, July 1984.

[45] W. Lindinger *et al.* Reactions of N_4^+ with O_2, CO_2, H_2, and D_2 and mobilities of N_4^+ in nitrogen. *Journal of Chemical Physics*, 68(6):2607–2611, March 1978.

[46] Robert N. Varney. Drift Velocity of Ion in Oxygen, Nitrogen, and Carbon Monoxide. *Physical Review*, 89(4):708–711, February 1953.

[47] Fons Rademakers Rene Brun. ROOT - An Object Oriented Data Analysis Framework. *Nuclear Instruments and Methods in Physics Research A*, 389(1-2):81–86, April 1997. doi: 10.1016/S0168-9002(97)00048-X. URL http://dx.doi.org/10.1016/S0168-9002(97)00048-X.

[48] F.I.G.M. Borges *et al.* Operation of gas proportional scintillation counters in a low charge multiplication regime. *Nuclear Instruments and Methods in Physics Research A*, 422(1-3):321–325, February 1999. doi: 10.1016/S0168-9002(98)00966-8. URL http://dx.doi.org/10.1016/S0168-9002(98)00966-8.

[49] L.M.P Fernandes *et al.* Primary and secondary scintillation measurements in a xenon gas proportional scintillation counter. *Journal of Instrumentation*, 5(09):P09006, September 2010. doi: 10.1088/1748-0221/5/09/P09006. URL http://stacks.iop.org/1748-0221/5/i=09/a=P09006.

[50] C. Tezuka *et al.* Electron diffusion and scintillation in xenon doped with hydrogen for high-pressure xenon time projection chamber. *IEEE Nuclear Science Symposium Conference Record*, 2:1157–1159, October 2004. doi: 10.1109/NSSMIC.2004.1462407. URL http://dx.doi.org/10.1109/NSSMIC.2004.1462407.

[51] R.K. Manchanda R.K. Sood *et al.* Transport and recombination of electrons in a high pressure proportional counter using different gas mixtures. *Nuclear Instruments and Methods in Physics Research A*, 595(3):605–615, August 2008. doi: 10.1016/j.nima.2008.08.021. URL http://dx.doi.org/10.1016/j.nima.2008.08.021.

[52] B. Ramsey A. Bolotnikov. Studies of light and charge produced by alpha-particles in high-pressure xenon. *Nuclear Instruments and Methods in Physics Research A*, 428(2-3):391–402, June 1999. doi: 10.1016/S0168-9002(99)00173-4. URL http://dx.doi.org/10.1016/S0168-9002(99)00173-4.

[53] M. Mimura *et al.* Intensity and time profile of recombination luminescence produced by an α-particle in dense xenon gas. *Nuclear Instruments and Methods in Physics research A*, 613(1):106–111, January 2010. doi: 10.1016/j.nima.2009.11.041. URL http://dx.doi.org/10.1016/j.nima.2009.11.041.

[54] The NEXT Collaboration. The NEXT-100 experiment for neutrinoless double beta decay searches (Conceptual Design Report). Technical report, June 2011.

[55] William R. Leo. *Techniques for Nuclear and Particle Physics Experiments.* Springer-Verlag, 2nd edition, February 1994.

[56] Syed Naeem Ahmed. *Physics and Engineering of Radiation Detection.* Academic Press, 1st edition, February 2007.